DEVELOPMENT, CHARACTERIZATION, AND MODELING OF $CuGaSe_2$/$Cu(In,Ga)Se_2$ THIN-FILM TANDEM SOLAR CELLS

By

JIYON SONG

A DISSERTATION PRESENTED TO THE GRADUATE SCHOOL
OF THE UNIVERSITY OF FLORIDA IN PARTIAL FULFILLMENT
OF THE REQUIREMENTS FOR THE DEGREE OF
DOCTOR OF PHILOSOPHY

UNIVERSITY OF FLORIDA

2006

Copyright 2006

by

Jiyon Song

ACKNOWLEDGMENTS

I would like to express my sincere gratitude to my supervisory committee chair, Dr. Sheng S. Li, for his guidance, support, and knowledge during the course of this dissertation. I would also like to thank Professors Gijs Bosman, Timothy J. Anderson, and Paul Holloway for serving on my supervisory committee.

I extend special thanks to Dr. Oscar D. Crisalle for his helpful advice on my research; Dr. Leon Chen, for supplying CIGS samples and depositing of ZnO layers; Dr. Rommel Noufi, for supplying CGS samples; Dr. Valentin Craciun, for his help on film characterization; and Dr. Jian Chen, for his help on Hall measurement.

I would like to extend my sincere appreciation to Dr. Seokhyun Yoon and Woo Kyoung Kim for their help on film characterization; and my colleagues, Drs Xuege Wang and Chia-Hua Huang, for their discussions on device characterization and fabrication.

I also thank Andre Baran, Ryan Kaczynski, Ryan Acher, Wei Liu, Chris Peek, Jihyun Kim, Yongho Choi, Joseph Park, Zivin Park, and Dr. Lei L. Kerr for their help and assistance. I could not have accomplished this work without their cooperation and help.

The author gratefully acknowledges the collaborations with the National Renewable Energy Laboratory and Energy Photovoltaics Inc. that provided the CGS and CIGS samples. Funding through the NREL high-performance photovoltaic program is gratefully acknowledged.

My deepest gratitude goes to my parents. I thank them for encouraging and supporting me in love and trust. I thank my sister and brother for always giving their best to support me. I dedicate this dissertation to them.

TABLE OF CONTENTS

page

ACKNOWLEDGMENTS..iii

LIST OF TABLES..viii

LIST OF FIGURES..ix

ABSTRACT..xii

CHAPTER

1 INTRODUCTION..1

2 FUNDAMENTALS OF CIS-BASED THIN-FILM TANDEM SOLAR CELLS..7

- 2.1 Overview of Solar Cell Technologies..7
  - 2.1.1 Introduction..7
  - 2.1.2 Crystalline Silicon Solar Cells..8
  - 2.1.3 Thin Film Solar Cells..9
- 2.2 Fundamental Solar Cell Parameters..12
- 2.3 Tandem Solar Cell Technologies..13
- 2.4 $CuGaSe_2$ Top Cell..15
- 2.5 Alternative Top Cells..17
  - 2.5.1 $CuInS_2$ Top Cell..17
  - 2.5.2 $CuGa(S_x,Se_{1-x})_2$ Top Cell..18
- 2.6 Alternative Buffer Layers for Wide Band-gap $CuGaSe_2$ Top Cell..18
  - 2.6.1 $Cd_{1-x}Zn_xS$ Buffer Layers..19
  - 2.6.2 ZnSe Buffer Layers..20
  - 2.6.3 Zn(Se,OH) Buffer Layers..21

3 DEVICE MODELING AND SIMULATION OF CIGS AND CGS SOLAR CELLS..28

- 3.1 Introduction..28
- 3.2 AMPS-1D Device Simulation Program..29
- 3.3 Modeling and Simulation of CIGS Cells..30
  - 3.3.1 Cell Structure and Material Parameters..30
  - 3.3.2 The Effect of CdS Layer Thickness on the CIS Cell Performance..31
  - 3.3.3 The Effect of Uniform Absorber Band-gap on the Cell Performance..32
  - 3.3.4 The Graded Band-gap Structure of CIGS Cells..32

3.3.5 Comparison with Experimental Data for CIGS Cells 33
3.4 Modeling and Simulation of CGS Cells 36
3.4.1 Cell Structure and Material Parameters 36
3.4.2 Comparison with Experimental Data for CGS Cells 37
3.5 Summary and Conclusions 37

4 NUMERICAL SIMULATION OF MECHANICALLY-STACKED CGS/CIGS TANDEM SOLAR CELLS 52

4.1 Introduction 52
4.2 Mechanically-Stacked CGS/CIGS Tandem Cell Structure 53
4.3 Simulation Method 54
4.4 The Effect of CGS Top Cell Thickness on the Performance of CIGS Bottom Cell 54
4.5 The Effect of CGS Absorber Thickness on the Performance of CGS/CIGS Tandem Cell 55
4.6 Summary and Conclusions 57

5 DEVELOPMENT, GROWTH, AND CHARACTERIZATION OF CHEMICAL-BATH-DEPOSITION CDZNS BUFFER LAYERS 62

5.1 Introduction 62
5.2 Development and Growth of CBD-CdZnS Buffer Layers 63
5.2.1 Chemical Bath Deposition Technique 63
5.2.2 Chemical Bath Deposition Condition 64
5.2.3 Definition of the Relative Zinc Content in the Buffer Film and in the CBD Solution 65
5.3 Characterization of CBD-CdZnS Thin Films 65
5.3.1 Thickness of CdZnS Films 65
5.3.2 Structural Analysis 66
5.3.3 Analysis of Surface Morphology 67
5.3.4 Optical Analysis 68
5.3.5 Electrical Analysis 69
5.4 Summary and Conclusions 70

6 FABRICATION AND MEASUREMENT SYSTEMS FOR CIGS AND CGS SOLAR CELLS 82

6.1 Introduction 82
6.2 Fabrication of CIGS and CGS Solar Cells 82
6.3 The Current-Voltage and Spectral Response Measurement Systems 83
6.3.1 Current-Voltage Measurement System 83
6.3.2 Spectral Response Measurement System 84

7 CURRENT-VOLTAGE AND SPECTRAL RESPONSE CHARACTERIZATIONS OF CIGS SOLAR CELLS WITH CDZNS BUFFER LAYERS 90

7.1 Introduction 90

7.2 The Effect of CIGS Absorber Surface Treatment by KCN on the Cell Performance 91
7.3 Current-Voltage and Quantum Efficiency of CIGS Cells with CdZnS Buffer Layers 92
  7.3.1 The Effect of Buffer Layer Thickness on the Cell Performance 92
  7.3.2 The Effect of Different Zn Compositions of CdZnS Buffer Layer on the Cell Performance 92
7.4 Summary and Conclusions 95

8 CURRENT-VOLTAGE AND SPECTRAL RESPONSE CHARACTERIZATIONS OF CGS SOLAR CELLS WITH CDZNS BUFFER LAYERS 105

8.1 Introduction 105
8.2 Surface Morphology of a CGS Film and a CdZnS Film on CGS 107
8.3 Current-Voltage Characteristics and Quantum Efficiency of CGS Cells with CdZnS Buffer Layers 108
8.4 Summary and Conclusions 111

9 SUMMARY AND FUTURE STUDIES 118

9.1 Summary and Conclusions 118
9.2 Future Studies 119

LIST OF REFERENCES 123

BIOGRAPHICAL SKETCH 130

LIST OF TABLES

Table page

2-1. The performance parameters of the best CIS-based solar cells. 23

2-2. The performance parameters of CIS-based thin-film tandem solar cells. 25

3-1. Material parameters of CIGS bottom cell. 40

3-2. Simulated performance parameters of the CIGS solar cells with a double band-gap grading profile. 44

3-3. The energy band-gap profile of the CIGS absorber layer used in simulation. 47

5-1. Estimated energy band gaps of CdZnS films for various relative Zn composition values (x). 80

5-2. Measured values of electrical resistance (R), resistivity (ρ), and conductivity (σ) for as-deposited CdZnS films on ITO coated glass substrates as a function of the relative Zn compositon x. 81

7-1. Performance of CdS/CIGS cells with and without a KCN treatment of the CIGS absorber layers. 96

7-2. Performance of CdZnS/CIGS cells with and without a KCN treatment of the CIGS absorber layers. 98

7-3. Performance parameters of CdZnS/CIGS cells as a function of different deposition times for a relative zinc composition x = 0.3 in the buffer layer. 100

7-4. Performance parameters of CdZnS/CIGS cells as a function of the relative zinc content x of the buffer layer. 101

8-1. Performance of CdS/CGS and CdZnS/CGS cells with and without KCN treatments on the CGS absorber layers (AM1.5G, 100 mW/cm^2). 114

8-2. The performance of CdS/CGS and CdZnS/CGS cells with KCN treatments on the CGS absorber layers (AM1.5G, 100 mW/cm^2). 117

LIST OF FIGURES

Figure page

2-1. Conduction and valence band diagram for a p-n heterojunction ZnO/CdS/CIGS solar cell. 22

2-2. Two-junction monolithically-cascaded and mechanically-stacked tandem solar cell structures. 24

2-3. Current-density voltage (J-V) characteristics of a solar cell in the dark and illuminated, defining the fundamental solar cell performance parameters: light-generated current density (J_L), short-circuit current density (J_{sc}), and open-circuit voltage (V_{oc}). Fill factor (FF) is determined by the maximum rectangle given by J_m and V_m. 26

2-4. Band diagrams with increasing Ga content of the $CuIn_{1-x}Ga_xSe_2$ absorber layer. ... 27

3-1. The schematic energy-band diagram of a typical ZnO/CdS/CIGS solar cell under equilibrium condition. 39

3-2. The photo-J-V curves for the simulated CIS cells with different thickness of CdS buffer layer for (a) 30 nm, (b) 60 nm, and (c) 80 nm. 41

3-3. Simulated performance parameters of the $CuInSe_2$ (E_g = 1.04 eV) and $Cu(In_{1-x},Ga_x)Se_2$ (E_g = 1.10, 1.18, and 1.22 eV) cells with different uniform absorber band-gap profiles; (a) V_{oc}, (b) J_{sc}, (c) FF, and (d) efficiency. 42

3-4. The schematic energy-band diagram of a CIGS cell with a double band-gap grading profile under equilibrium condition. 43

3-5. The photo-J-V curves for the simulated results (solid and dashed lines) and the reported experimental data (solid circles). 45

3-6. The normalized QE for the simulated results (solid line) and the reported experimental data (solid circles). 46

3-7. The photo-J-V curves for the simulated results (solid line) and the published data (solid circles). 48

3-8. A comparison of the performance parameters for the simulated results (circles) and the published data (triangles). 49

3-9. The schematic energy-band diagram for a CGS cell under equilibrium condition. . 50

3-10. The photo-J-V curve for the simulated results and the published data. 51

4-1. A schematic of a four-terminal mechanically-stacked CGS/CIGS tandem cell structure. 58

4-2. Performance parameters of CIGS bottom cell under working CGS top cell as a function of CGS absorber thickness. 59

4-3. Efficiencies of CGS/CIGS tandem cell, CGS top cell, and CIGS bottom cell under top cell as a function of CGS top cell absorber thickness. 60

4-4. Simulated photo-J-V curves of a CGS top cell and a CIGS bottom cell under the CGS top cell for a CGS/CIGS tandem cell with an efficiency of 25.22%. 61

5-1. Film thickness as a function of deposition time for CdZnS films with relative zinc compositions x = 0, 0.3, and 0.5. 72

5-2. Film thickness variation as a function of relative zinc composition x for CdZnS films with deposition time of 50 minutes. 73

5-3. Powder XRD patterns of CdZnS films deposited on SLG with relative zinc composition x = 0 (film thickness d ≈ 200 nm), x = 0.3 (d ≈ 100 nm), and x = 0.5 (d ≈ 150 nm). 74

5-4. Grazing incidence XRD patterns of CdZnS films, deposited on Mo, with relative zinc compositions x = 0, 0.3, and 0.5. 75

5-5. SEM micrographs of the surface of a $Cd_{1-x}Zn_xS$ thin film with relative zinc composition x = 0 (CdS). 76

5-6. SEM micrographs of the surface of a $Cd_{1-x}Zn_xS$ thin film with relative zinc composition x = 0.3. 76

5-7. SEM micrographs of the surface of a $Cd_{1-x}Zn_xS$ thin film with relative zinc composition x = 0.5. 76

5-8. Optical transmittance spectra of CdZnS films with relative zinc composition x = 0.3 for different film thickness. 77

5-9. Optical transmittance spectra of CdZnS films with relative zinc compositions x = 0 (thickness d ≈ 200 nm) and x = 0.3 (d ≈ 100 nm). 78

5-10. Plots of $(\alpha h\nu)^2$ versus $h\nu$ for CdZnS films with relative zinc compositions x = 0 (thickness d ≈ 200 nm), x = 0.3 (d ≈ 100 nm), and x = 0.5 (d ≈ 150 nm). 79

6-1. Solar cell structure used to fabricate a ZnO/CdZnS/CIGS (or CGS) cell. 87

6-2. A completely finished CIGS cell with Ni/Al top contact. 88

6-3. A cross-sectional SEM image of the ZnO/CdZnS/CIGS/Mo/SLG cell (10,000X). 89

7-1. Quantum efficiency for the CdS/CIGS solar cells shown in Table 7-1 (Device ID: 39#8 and 21#4). 97

7-2. Photo-J-V characteristics of CdZnS/CIGS cells using different deposition times and relative zinc composition x = 0.3. The CBD-grown CdZnS buffer layers were fabricated with deposition times of 40 min (A), 50 min (B), and 60 min (C), in an 85 °C bath. 99

7-3. Performance parameters of CdZnS/CIGS cells as a function of the relative zinc content x (graphical representation of the data given in Table 7-4). 102

7-4. Photo-J-V characteristics of CdZnS/CIGS cells with different relative zinc contents x = 0 (A), x = 0.1 (B), x = 0.2 (C), x = 0.3 (D), x = 0.4 (E), and x = 0.5 (F). 103

7-5. Quantum efficiency comparison between a CdS/CIGS solar cell (A), and CdZnS/CIGS solar cells with relative zinc composition x = 0.2 (C) and x = 0.5 (F). 104

8-1. SEM micrograph of the surface of a CGS film etched with a 10% KCN solution (10,000X). 112

8-2. SEM micrograph of the surface of a $Cd_{1-x}Zn_xS$ film (x = 0.1) deposited on a CGS absorber etched with a 10% KCN solution (10,000X). 112

8-3. AFM image of the surface of a CGS film etched with a 10% KCN solution. 113

8-4. AFM image of the surface of a $Cd_{1-x}Zn_xS$ film (x = 0.1) deposited on a CGS absorber etched with a 10% KCN solution. 113

8-5. Photo-J-V characteristics of a CdS/CGS cell and a CdZnS/CGS cell with relative zinc composition x = 0.3. 115

8-6. Quantum efficiency vs. wavelength for the cells shown in Figure 8-5. 116

Abstract of Dissertation Presented to the Graduate School
of the University of Florida in Partial Fulfillment of the
Requirements for the Degree of Doctor of Philosophy

DEVELOPMENT, CHARACTERIZATION, AND MODELING OF $CuGaSe_2/Cu(In,Ga)Se_2$ THIN-FILM TANDEM SOLAR CELLS

By

Jiyon Song

August 2006

Chair: Sheng S. Li
Major Department: Electrical and Computer Engineering

Device modeling and numerical simulation of mechanically-stacked $CuGaSe_2/Cu(In_{1-x},Ga_x)Se_2$ (CGS/CIGS) tandem solar cells were carried out in this work using AMPS-1D (analysis of microelectronic and photonic structures) device simulation program. The CGS/CIGS two-junction tandem cell consists of a CIGS bottom cell using a double graded band gap CIGS absorber layer and a CGS top cell with a uniform band gap CGS absorber layer. Simulated photo-current-voltage and spectral response (quantum efficiency) characteristics for both single-junction CIGS and CGS cells were found in good agreement with the experimental data. Simulation results revealed that a CGS/CIGS tandem cell with a conversion efficiency of 25% under AM1.5G condition could be achieved using a CGS top cell with an efficiency of over 16% and an optimized CIGS bottom cell structure.

To determine the effect of the relative content of zinc, x, in the chemical bath deposition (CBD) bath on the $Cd_{1-x}Zn_xS$ (CdZnS) thin-film properties, the structural, surface morphological, optical, and electrical characterizations are conducted by using

XRD, SEM, spectrophotometer, and resistivity measurements. The degree of crystallinity in the film decreases with increasing relative Zn content x, leading to an amorphous structure at a concentration level of $x = 0.5$. CdZnS films with film thickness less than 50 nm and relative Zn composition $x = 0.3$ show better than 80% transmittance for wavelengths longer than 600 nm. Band gap increases with increasing Zn content x. The results reveal that a CdZnS film with a relative Zn content of $x = 0.3$ in the CBD bath is an excellent candidate as a buffer-layer material for the CIGS and CGS cells.

In this study $Cd_{1-x}Zn_xS$ buffer layers were deposited on CIGS absorber films with relative Zn content $x = 0$ (CdS), 0.1, 0.2, 0.3, 0.4, and 0.5 in the CBD bath and on CGS absorber films with $x = 0$ and 0.3. In both the CIGS and CGS cases, the experimental results show that it is beneficial to pre-treat the absorber layer with a 10% KCN solution before CBD growth. A CdZnS/CIGS cell with relative Zn composition of $x = 0.2$ achieves an efficiency of approximately 13% under AM1.5G condition, showing improved V_{oc}, J_{sc}, and FF values as compared to the CdS/CIGS cells and other CdZnS/CIGS cells with different Zn content. For CGS cells, it is demonstrated that the CdZnS buffer layer improves V_{oc} value which is attributed to the reduced conduction band discontinuity at the junction. It is also observed that the CdZnS/CGS cell has increased the photocurrent generation at shorter wavelengths ($\lambda < 500$ nm), resulting in a higher J_{sc} value than the CdS/CGS cells due to higher quantum efficiency.

CHAPTER 1
INTRODUCTION

The sun has been constantly emitting energy for over five billion years. Astronomers estimate it will continue for another five billion years. Solar energy, which is the solar radiation that reaches the earth, can be used to provide heat, light, hot water, electricity, and heating for homes, businesses, and industry. Solar cells are photovoltaic devices that can directly convert sunlight into electricity which can be used almost anywhere. The solar cells can provide low cost and alternative solutions to fossil fuels for terrestrial power generation, and are clean and environmental friendly. The simplest solar cells power watches, calculators, radios, lanterns, and other small battery charging applications, while large solar panels or modules can provide lighting to the houses and feed power to the utility electric grids. Thin-film photovoltaic (PV) technologies have been developed to reduce the cost of photovoltaic systems. Thin film PV materials show promise for reducing the materials requirements and manufacturing costs. At present, one of the most promising semiconductor materials for thin-film solar cells is copper indium gallium diselenide ($CuIn_{1-x}Ga_xSe_2$ or CIGS) which can utilize the direct band-gap energy between $E_g = 1$ eV for copper indium diselenide ($CuInSe_2$ or CIS) and $E_g = 1.7$ eV for copper gallium diselenide ($CuGaSe_2$ or CGS). So far, the best CIGS thin-film solar cell has achieved a maximum conversion efficiency of 19.5% AM1.5G [1]. However, the maximum theoretical efficiency for a single-junction CIGS solar cell is 27.5% AM 1.5G [2]. The measured conversion efficiency for the CIGS cell is still below the theoretical prediction. One way to improve efficiency is to use two or more layers of absorber materials with different band gaps. The higher band gap absorber material can be used in the top cell, absorbing high energy photons while allowing lower energy photons to be absorbed by the lower band gap bottom cell. This cell structure, called the two-junction tandem cell, can have more than one electric field which results in a much higher efficiency.

Exploiting the recent research and progress of CIGS thin-film technologies and the achievements of tandem cells in space applications, the two-junction tandem solar cell incorporating with CIGS as a bottom cell and CGS as a top cell can be realized along with research issues that need to be addressed. The CIGS and CGS offer the optimal band-gap energy values in the combination of a two-junction tandem configuration and the close lattice parameters.

A main challenge for improving efficiency of the wide band-gap materials, such as $CuGaSe_2$ (CGS), is the open-circuit voltage, V_{oc}. In order to produce a favorable conduction band offset, which contributes to enhancing V_{oc}, at the buffer/absorber interface layer, an alternative buffer layer which has a wider band gap than CdS should be developed. The $Cd_{1-x}Zn_xS$ (CdZnS) ternary system with its band-gap energy varying between 2.4 eV for the cadmium sulfide (CdS) and 3.8 eV for the zinc sulfide (ZnS), has good lattice match to CGS and can be utilized as a buffer layer. Due to the larger band gap of CdZnS film it could increase the quantum efficiency of CIGS and CGS solar cells in the shorter wavelengths. In this research, we present a study of the CdZnS film growth and characterization, and evaluate the impact of CdZnS buffer layers on the performance of CIGS and CGS cells. Modeling and simulation of a mechanically-stacked CGS/CIGS tandem solar cell have been carried out in this research.

The objectives of this research are (1) to develop device models for the CGS/CIGS tandem solar cells using the AMPS-1D device simulation program to describe the CGS top and CIGS bottom cells, (2) to characterize the physical properties of CdZnS thin films deposited via chemical bath deposition (CBD), (3) to determine the effect of the relative content of zinc on those properties, and (4) to establish the advantages of using the CdZnS thin-film material as a buffer layer for CIGS and CGS solar cells.

Chapter 2 briefly reviews the solar cell technologies based on two categories of crystalline silicon and thin film solar cells. The fundamental solar cell parameters are determined from the dark and illuminated current-voltage curves for evaluating the cell performance. The technologies of tandem solar cell devices based on the mechanically-stacked and monolithically-cascaded cell structures are depicted. The CGS solar cell used as the top cell of a CGS/CIGS two-junction tandem cell is investigated in this research. Additionally, two $CuInS_2$ and $CuGa(S_x,Se_{1-x})_2$ cells are presented as alternative top cells in this chapter. Furthermore, wide band-gap materials such as CdZnS, ZnSe, and Zn(Se,OH) are investigated for use as alternative buffer layers to replace the CdS for the CGS top cell.

In Chapter 3, device modeling and numerical simulation on the performance of single-junction $CuInGaSe_2$ (CIGS) and $CuGaSe_2$ (CGS) solar cells are presented. The CIGS and CGS cells were used as a bottom cell and a top cell for the tandem solar cell modeling to be depicted in Chapter 4. The AMPS-1D (Analysis of Microelectronic and Photonic Structures) device simulation program is employed as a computer simulation tool for the CGS/CIGS tandem solar cells. The cell structures and material parameters for each layer of CIGS and CGS cells are depicted. In particular, for the CIGS bottom cell, a double graded band-gap profile which has a grading in the space charge region and in the backside of the CIGS absorber layer is presented and discussed. In addition, the effects of CdS buffer layer thickness on the CIS cell performance and of various uniform CIGS absorber layer band gaps using different Ga contents on the CIGS cell performance are investigated in this chapter. For the CGS top cell a uniform band gap profile for the CGS absorber layer was modeled with low defect density in the absorber region to produce a high-efficiency top cell in the tandem cell structure. To verify the validity of device modeling, the simulated performance characteristics, such as photo-current density-voltage and spectral response curves, of the CIGS and CGS cells were compared to the experimental data, and excellent agreement was obtained from this study. For the CIGS bottom cells, detailed investigation was made to compare the simulated and experimental values using various band gap grading structures in the absorber layers.

In Chapter 4, a numerical simulation of CGS/CIGS two-junction tandem solar cell is presented. Based on the results of single-junction CIGS and CGS cell simulations presented in Chapter 3, a two-junction four-terminal mechanically-stacked CGS/CIGS tandem solar cell structure was established. To investigate the performance of CIGS bottom cell underneath the CGS top cell, as a function of CGS absorber layer thickness up to 2 μm of the top cell, the performance of CIGS bottom cell under the top cell with various thicknesses was simulated, and the results are shown and discussed in this chapter. Furthermore, simulations of the performance of CGS top cell as a function of the CGS absorber thickness were carried out in this study. Finally, the conversion efficiency of CGS/CIGS tandem cell was obtained by using the simulation results of the CIGS bottom cell under the CGS top cell.

In Chapter 5, the growth and characterization of $Cd_{1-x}Zn_xS$ (CdZnS) thin-film buffer layers deposited via chemical bath deposition (CBD) are presented. The CBD process technique and deposition conditions are also described. Zn composition parameter in the CBD bath (not on the film) x_{bath} was simplified by assuming $x_{bath} = x$ (*i.e.*, x is the Zn mole fraction in $Cd_{1-x}Zn_xS$ film). The CdZnS films were grown on soda lime glasses for characterization of film compositions and optical properties. The thickness variation of CdZnS films as a function of Zn content up to $x = 0.5$ was investigated. Structural, surface morphological, optical, and electrical analyses on the CdZnS films with different Zn contents were performed by using x-ray diffraction (XRD), scanning electron microscopy (SEM), spectrophotometer, and resistivity measurements. Studies of the physical properties of CdZnS depicted in this chapter would yield the range of Zn content in the CdZnS buffer layers for the CIGS and CGS solar cells presented in Chapter 7 and 8.

In Chapter 6, the fabrication process of CIGS and CGS solar cells is described. The cell structure used in the fabrication of ZnO/CdZnS/CIGS (or CGS) solar cell on the Mo/glass substrate, the cross-sectional SEM image showing each layer of CIGS cell, and a finished CIGS cell with Ni/Al front contact are presented. This chapter also depicts the current-voltage (I-V) and spectral response (quantum efficiency) measurement systems for the device characterization of CIGS and CGS solar cells.

Chapter 7 presents the photo-I-V and quantum efficiency (QE) measurements of CIGS solar cells deposited with $Cd_{1-x}Zn_xS$ buffer layers of various Zn contents (*i.e.*, $x = 0$ (CdS) to $x = 0.5$). First, KCN surface treatment was used on the CIGS absorber film before depositing a buffer layer to investigate the effects of KCN treatment on the CIGS cell performance. The results of performance parameters and QE are presented and compared to the cell performance without KCN treatment. Second, the effects of CdZnS buffer layer thickness on the cell performance are discussed. Third, the CIGS cells deposited with CdZnS buffer layers of different Zn contents were fabricated and characterized by photo-I-V and QE measurements. The short-circuit current density (J_{sc}), open-circuit voltage (V_{oc}), fill factor (FF), conversion efficiency (η), and the QE values in the short wavelength regime are analyzed in this chapter. Finally, the performance of the CdZnS/CIGS cells is compared to that of the CdS/CIGS cells.

Chapter 8 presents the device characterization of CGS top cells using $Cd_{1-x}Zn_xS$ buffer layers with Zn content $x = 0, 0.3$. In addition, the surface characterizations by SEM and AFM (atomic force microscope) were carried out to investigate the surface morphology of CGS absorber films with KCN treatment and the CdZnS buffer film deposited on the CGS absorber treated by KCN. The images taken are shown in this chapter. KCN surface treatment on the CGS absorber film before depositing a buffer layer was performed to investigate the effects of absorber treatment with KCN on the CGS cell performance. The results of performance parameters of the cells treated with KCN are compared to the cell performance without KCN treatment. The CdZnS/CGS cells were fabricated and characterized by photo-I-V and QE measurements. The photo-I-V and QE curves of this cell were compared to those of CdS/CGS cells. A comparison of the V_{oc} and photo-current generation in the shorter wavelengths for the CGS cells deposited with CdZnS and CdS buffer layers is also discussed in this chapter.

Chapter 9 gives the summary and conclusions on the modeling and simulation results for the single-junction CIGS and CGS cells, and the CGS/CIGS tandem cells, the characterization results for the CdZnS buffer layers, CIGS and CGS solar cell devices. Future studies for the low cost, high performance CIGS and CGS thin-film solar cells as well as CGS/CIGS tandem solar cells are also presented in this chapter.

CHAPTER 2
FUNDAMENTALS OF CIS-BASED THIN-FILM TANDEM SOLAR CELLS

2.1 Overview of Solar Cell Technologies

2.1.1 Introduction

A solar cell, which converts the solar energy (sunlight) directly into electricity, is known as the photovoltaic (PV) device. The PV effect was discovered by Edmond Becquerel in 1839. Solar cells can be fabricated from a wide variety of semiconductors such as silicon, GaAs, InGaP, CdTe, and $CuInSe_2$ material systems.

The fundamental physical process of the PV effect in a bulk semiconductor is described as follows: When the incident photons with energy greater than the band-gap energy of the semiconductor are absorbed in a semiconductor, electron-hole pairs are generated in a solar cell via internal photovoltaic effect. Solar cells are formed using a Schottky barrier, a metal-insulator-semiconductor (MIS) structure, or a p-n heterojunction solar cell formed by utilizing two semiconductor materials with different band-gap energies and opposite dopant impurities such as a p^+-InGaP/n-GaAs, p^+-GaAs/n-Ge, n-CdS/p-CdTe, or an n-CdS/p-CIGS materials.

The energy band diagram for an n-ZnO/n-CdS/p-CIGS n-p heterojunction solar cell is shown in Figure 2-1. The CIGS denotes $Cu(In_{1-x},Ga_x)Se_2$ absorber material. As shown in this figure, photons with energy smaller than 3.3 eV (E_g = 3.3 eV is the band gap for ZnO) will pass through the ZnO window layer. Some photons with energies of 2.4 eV < E_{photon} < 3.3 eV (E_g = 2.4 eV for CdS) will be absorbed in the CdS buffer layer, but most will reach the CIGS absorber layer. CIGS and CdTe are direct band-gap semiconductor materials which have large optical absorption coefficients (> 10^5 cm^{-1}). The optical absorption depth is very small (*i.e.*, $\alpha^{-1} \sim 0.1$ μm) in the CIGS absorber layer. Therefore, the majority of electron-hole pairs are generated in the space charge region (SCR) of the CIGS solar cells. When the generation occurs within the SCR, these photo-generated carriers are swept out by the built-in electric field in the SCR. The holes and electrons are swept to the p- and n- quasi-neutral region (QNR), and are collected at the top and bottom contacts of solar cell as electric current in the external circuits. The electron- hole pairs generated outside the SCR, either in the n- or p- QNR, are minority carriers which must traverse to the SCR by the diffusion process. This diffusion transport process depends on the quality of semiconductor materials, which can be determined by the minority carrier lifetimes or diffusion lengths. The absorption in the CdS buffer layer can be reduced by thinning this buffer layer or using an alternative buffer layer material such as $Cd_{1-x}Zn_xS$, ZnSe, or Zn(Se,OH) with larger band-gap energy, as will be introduced in this chapter. Detailed discussion of using $Cd_{1-x}Zn_xS$ buffer layers in CGS and CIGS solar cells will be given in Chapters 7 and 8, respectively.

2.1.2 Crystalline Silicon Solar Cells

Silicon is the most extensively studied semiconductor material, and was the first commercially used solar cell material. Historically, crystalline silicon (*c*-Si) has been used in the fabrication of most solar cells. The first silicon solar cell with a conversion efficiency of 6% air mass zero (AM0) was demonstrated in 1954 for space applications. Currently, single- and multi-crystalline- silicon materials are used in the industry for production of solar panels and modules for a wide variety of commercial use, and multi-crystalline silicon technology has been emerged as the main trend in *c*-Si solar cell manufacture. Single and multi-crystalline silicon solar cells with one-sun conversion efficiencies in the range of 14 ~ 25% AM1.5G (100 mW/cm^2 input sunlight) have been demonstrated utilizing various fabrication processes and device structures. Single crystalline silicon as an indirect semiconductor material has relatively low optical absorption coefficients, which need a relatively thick layer (d = 250 - 400 μm) to absorb the sunlight. In spite of these disadvantages, it has produced stable solar cells with relatively good efficiencies. Moreover, it utilizes matured processing technology, which has been developed based on the extensive knowledge of the microelectronics industry.

2.1.3 Thin Film Solar Cells

In the solar cell industry, the efforts for low-cost, large-scale solar cell manufacture have been driven by the high costs of *c*-Si wafers. For low-cost and large-scale terrestrial photovoltaic power generation applications, the most promising and common semiconductor materials are amorphous silicon (*a*-Si) or the polycrystalline materials such as cadmium telluride (CdTe) and copper indium (gallium) diselenide (CIS or CIGS). These absorber materials for thin film solar cells have strong optical absorption coefficients, and thus they require only a few micrometers thick of material. Therefore, the costs for materials are significantly reduced. In addition, they allow large area deposition. The thin film semiconductor layers can be grown on a wide variety of low-cost substrate materials such as Mo-coated soda-lime glass, flexible plastic, ceramic, graphite, aluminum, polymer, or stainless steel sheet. The junction is formed as a p-i-n cell structure in *a*-Si thin film solar cells, while it is formed as a p-n heterojunction structure using a thin n-type cadmium sulphide (CdS) buffer layer deposited on CdTe, CIS, or CIGS absorber layers.

Amorphous silicon (*a*-Si) is the most extensively developed and the first commercial solar cell material using thin film technologies. The *a*-Si solar cells, which use a p-i-n cell structure, encounter a significantly degraded output power when they are exposed to the sunlight via the Staebler-Wronski effect [3]. Hydrogen passivation can reduce this effect. The degradation problem in *a*-Si has led to the development of double- and triple-junction tandem solar cells by incorporating with Si- Ge alloys. However, the processing steps for the triple junction *a*-Si solar cells are more complex. A single-junction *a*-Si:H solar cell with a conversion efficiency of around 10-11% AM1.5G and an *a*-Si/*a*-SiGe/*a*-SiGe triple-junction tandem solar cell with over 14% AM1.5G have been manufactured for commercial applications. Recently, a two-terminal *a*-Si:H/poly-Si and a proto-type four-terminal *a*-Si:H/poly-Si tandem solar cells have achieved conversion efficiencies of 15.04% AM1.5G and 21% AM1.5G, respectively.

Cadmium telluride (CdTe) is a semiconductor material with nearly ideal photovoltaic properties due to its band-gap energy of 1.4 eV, which is almost perfectly matched to the peak of solar spectrum. In addition, it can be easily deposited due to the congruent evaporation of this compound, and stoichiometry can be adjusted by simple annealing procedures. These properties provide low-cost manufacturing processes for high-efficiency modules. A major limitation is the toxicity of cadmium (Cd) containing material, which makes the material problematic on a market. Currently, the word-record conversion efficiency of 16.5% for CdTe thin film solar cell has been achieved.

A wide range of research of new semiconductor materials for thin film devices has been extended to the investigation of ternary and quaternary compounds. The developments of $CuInSe_2$ (CIS) have shown the promising potential of this material. The CIS absorber material is a direct band-gap material with high optical absorption coefficients in the visible spectrum of the incident sunlight. It shows excellent photovoltaic properties as a polycrystalline thin film absorber layer. As a result, the CIS material is the most promising candidate for high-efficiency thin-film solar cells applications. The CIS has a band gap energy of ~ 1 eV. Adding Ga to CIS, forming $CuIn_{1-x}Ga_xSe_2$ (CIGS) alloy, will increase the band-gap energy up to ~ 1.7 eV for $CuGaSe_2$ (CGS), and thus it enhances the open-circuit voltage (V_{oc}) of the solar cells. It has been experimentally observed that CIGS solar cells do not follow the theoretically predicted efficiency increase with band-gap energy. The highest conversion efficiency achieved for a CIGS thin film solar cell is around 19.5 % AM1.5G, which has about 30% of Ga in the $CuIn_{1-x}Ga_xSe_2$ absorber with band-gap energy of around 1.15 eV. Table 2-1 shows the device performance parameters for a CIS-based thin-film solar cell with the highest conversion efficiency made to-date.

It has been known that photons in the different wavelengths of the solar spectrum can be used to convert the sunlight into electricity effectively by stacking several single-junction solar cells with different band gap materials. Figure 2-2 illustrates a two-junction monolithically-cascaded and a mechanically-stacked tandem solar cell structure. The tandem cell concept is especially suitable for thin film solar cells, and other systems such as *a*-Si:H/*a*-Si-Ge:H, *a*-Si:H/$CuInSe_2$, or $CuGaSe_2/CuInSe_2$ have also been reported. In particular, polycrystalline thin films of chalcopyrite semiconductor materials are very promising and attractive candidates for low-cost high-performance tandem solar cells with relatively advanced technologies. Table 2-2 shows several polycrystalline CIS-based thin-film tandem solar cell structures which have been recently developed, along with their device performance parameters. Tandem solar cells are reviewed in detail in section 2.3 in this chapter. For a two-junction CGS/CIGS tandem solar cell using $CuGaSe_2$ absorber as top cell is reviewed along with possible alternative top cells using $CuInS_2$ and $CuGa(S_x,Se_{1-x})_2$.

2.2 Fundamental Solar Cell Parameters

The performance of a solar cell under illumination can be depicted by the current-voltage characteristics. If typical current-voltage curves of a p-n junction diode in the dark and under illumination are considered, solar cell parameters can be determined. Figure 2-3 shows current-density voltage (J-V) characteristics of a solar cell in the dark and under illumination. The light current density-voltage characteristics of a solar cell can be described by the diode equation, which is given by

$$J = J_o\left[e^{\frac{qV}{nk_BT}} - 1\right] - J_L, \tag{2.1}$$

where J_o is the reverse bias saturation current density, J_L is the light generated current density, k_B is Boltzmann's constant, T is temperature in K, q is an electron charge, and n is the diode quality factor ($n = 1$ for an ideal diode). The dark current density J_{dark} ($J_L = 0$ in the above equation) is described by

$$J_{dark} = J_o\left[e^{\frac{qV}{nk_BT}} - 1\right]. \tag{2.2}$$

When two parasitic resistances such as series resistance R_s and shunt resistance R_{sh} are included for a non-ideal solar cell, the diode equation (2.1) becomes

$$J = J_o\left[e^{\frac{q(V-JR_s)}{nk_BT}} - 1\right] + \frac{(V - JR_s)}{R_{sh}} - J_L. \tag{2.3}$$

R_s and R_{sh} reduce the fill factor FF, for an efficient cell, small R_s ($R_s = 0$ for the ideal case) and large R_{sh} ($R_{sh} = \infty$ for the ideal case) are desirable.

The short-circuit current density J_{sc}, which is obtained for $V = 0$, for the ideal case, is equal to the light generated current density J_L. The open-circuit voltage V_{oc}, which is obtained for $J = 0$, for the ideal case, can be derived by

$$V_{oc} = \frac{k_B T}{q} \ln\left[\frac{J_{sc}}{J_o} + 1\right]. \tag{2.4}$$

The cell power density is given by

$$P = JV. \tag{2.5}$$

The solar cell is operated under conditions which give the maximum power output. The maximum area $P_m = J_m V_m$ for a given current-voltage curve defines the fill factor FF, which is shown below

$$FF = \frac{J_m V_m}{J_{sc} V_{oc}}. \tag{2.6}$$

The energy conversion efficiency η_c of the solar cell, which is defined by

$$\eta_c = \frac{J_m V_m}{P_{in}} = \frac{J_{sc} V_{oc} FF}{P_{in}}, \tag{2.7}$$

where P_{in} is the incident light power density.

J_{sc}, V_{oc}, FF, and η_c are four key parameters which determine the performance characteristics of a solar cell. The standard test condition for solar cells is the Air Mass 1.5 Global (AM1.5G) spectrum, an incident light power density of 100 mW/cm^2, and at a temperature of 25°C. Further information on the basic device physics and electrical characteristics of a p-n junction solar cell can be found in Li [4].

2.3 Tandem Solar Cell Technologies

For terrestrial applications, the optimal band-gap energy for a two-junction tandem solar cell is in the range of 1.6 to 1.8 eV for the top cell, and 0.9 to 1.2 eV for the bottom cell [5-7]. Applicable range of optical band gaps for the top cell materials may vary in the range of 1.45 to 1.80 eV with conversion efficiencies over 15%. Calculated optimum band gaps on the basis of maximum daily energy density were found to be 1.72 ± 0.02 eV for the top cell and 1.14 ± 0.02 eV for the bottom cell [8]. These optimum band gaps have been studied for the two-terminal monolithic two-junction tandem devices using ideal device model.

Monolithic tandem solar cells require precisely controlled epitaxial growth, while mechanically stacked cells need complicated antireflection coatings to provide better optical coupling. The difficulty of series-connected cells is that the performance is determined by the bad cell in the tandem system. For the monolithic cascaded tandem devices with a two-terminal, the current flowing from the top cell must match to that passing through the bottom cell. Since the short-circuit current is mainly determined by the short-circuit current of the bad cell, it is thus necessary to explore a structure where the top and bottom cells have approximately the same short-circuit current for maintaining a good conversion efficiency of the tandem devices.

The critical path to the design of a two-terminal monolithic tandem cell is the development of an optimal tunnel junction, which electrically connects the top and bottom cells. A highly doped p^+/n^+ tunnel junction is an attractive approach to provide a shorting low-resistance intercell ohmic contact. A poor quality tunnel junction can greatly reduce the fill factor of a monolithic tandem cell. The problems of tunnel junction are related to the energy band gap and doping densities. The diffusion of the tunnel junction during the growth of top cell can affect the quality of tunnel junction and top cell with a wide variety of defects.

For mechanically-stacked four-terminal tandem cells, P. Meyers *et al.* reported a polycrystalline CdTe/CIS tandem cell with an efficiency of 9.9% [9]. A GaAs/CIS mechanically-stacked tandem cell with an efficiency of 23.1% was reported [10]. For the monolithic two-terminal tandem solar cells, CdTe/CIS tandem cell with an efficiency of 3% [11] and *a*-Si:H/CIS tandem cell with an efficiency of 5.8% [12] have also been reported. Studies of tandem solar cells using device simulation program such as ADEPT [13,14] and AMPS-1D [15,16] have been reported by various research groups. Theoretical studies have shown that in comparison to mechanically-stacked tandem solar cells, monolithic tandem cells have lower efficiency. However, if the process for the growth of top and bottom cells is simple, then the monolithic tandem cells would be more favorable. The performance of an ideal tandem solar cell structure using a CdZnS/CGS top cell and a CdZnS/CIS bottom cell at AM1.5G condition has a calculated conversion efficiency of 33.9% [17], which is much higher than the experimental values reported in the literature.

2.4 $CuGaSe_2$ Top Cell

Cu-chalcopyrite semiconductor materials of $Cu(In_{1-x},Ga_x)(Se_y,S_{1-y})_2$ provide a wide range of band gaps from 1.0 eV for $CuInSe_2$ to 2.4 eV for $CuGaS_2$. A direct band-gap material with E_g = 1.68 eV at room temperature and very high optical absorption coefficients [18], the $CuGaSe_2$ (CGS) has received considerable attention as a promising candidate for the absorber material of the top cell in a two-junction tandem solar cell structure of thin film photovoltaic devices. The world-record total-area conversion efficiency of 10.2% for a surface-modified CGS solar cell has been achieved with the performance parameters of V_{oc} = 0.823 V, J_{sc} = 18.61 mA/cm^2, and FF = 66.77% [1].

The critical issue of CGS solar cells is the low open-circuit voltage. The open-circuit voltage (V_{oc}) of $CuInSe_2$ (CIS) and $Cu(In_{1-x},Ga_x)Se_2$ (CIGS) solar cells can approximately be described by $V_{oc} \approx (E_g/q) - 0.5$ V, where E_g is the band-gap energy of the absorber and q is the electron charge [19]. Open-circuit voltage of 1.2 V is possible for CGS solar cells based on this formula. All reported performance parameters lie below the theoretical limit of an ideal CGS solar cell [2]. It was reported that the limitation of the high-efficiency CGS solar cells comes from the tunneling current at the interface of the CdS and CGS layers [20]. CGS shows a very high net hole concentration in the range of 10^{18} cm^{-3}. Such a high net hole concentration in the CGS absorber leads to a very thin width of the space charge region (SCR) in the absorber layer. The diffusion length for the minority carriers in the absorber should be long enough to achieve a high photocurrent density. It has been shown that the open-circuit voltage is related strongly by the characteristic tunneling energy described by $E_{oo} = (q\hbar / 2) [N_A / (m^*\varepsilon)]^{1/2}$ [19], where N_A is the net hole concentration and m* is the effective tunneling mass. The low values of tunneling energy produce the best devices. The improved efficiency by the use of Ga-rich absorbers was achieved by explaining the reduction of the net hole concentration in the range of 10^{16} cm^{-3} and the decrease of the tunneling rate [19]. For a further decrease of the tunneling energy, air annealing or modification of the CdS deposition temperature was considered [21]. To obtain a high photo-generated current density it is suggested that the net hole concentration should be reduced to ~ 10^{16} cm^{-3} to increase the width of the depletion region in the absorber side [20].

CdS has been widely used as a buffer layer for chalcopyrite solar cells. CdS/CGS solar cell structure has a cliff in the conduction band, which reduces the open-circuit voltage [21]. $Cd_{1-x}Zn_xS$ buffer layers with band gaps ranging from 2.4 eV (CdS) to 3.8 eV (ZnS) and a ZnSe buffer layer with band gap of 2.7 eV form a favorable conduction band alignment with CGS absorber layer [22], as several papers on these wide band gap buffer materials have been published recently [23-25]. Alternative buffer layers, such as $Cd_{1-x}Zn_xS$, ZnSe, and Zn(Se,OH), for the replacement of a CdS buffer layer for the CIGS and CGS solar cells are discussed in detail in section 2.6 in this chapter.

2.5 Alternative Top Cells

2.5.1 $CuInS_2$ Top Cell

Another promising absorber material with band gaps beyond 1.5 eV for the high-efficient top cell in tandem solar cells is to realize high open-circuit voltage devices using ternary wide band gap absorber $CuInS_2$. $CuInS_2$ with its direct band gap between 1.50 eV [26] and 1.55 eV [27], which matches with the solar spectrum, also has high optical absorption coefficient of 10^5 cm^{-1} [28]. The maximum theoretical efficiency of $CuInS_2$ reaches 28.5% compared to 26% of CGS [2]. However, the highest efficiencies reported of $CuInS_2$ solar cells so far are 12.2% active area efficiency reported in 1996 [29] and 11.4% total area efficiency reported in 2001 [30]. An 11.4% efficiency of $CuInS_2$ solar cell was prepared by a rapid thermal process (RTP) for a $ZnO/CdS/CuInS_2/Mo$/glass cell structure with an antireflection coating. This solar cell has an open-circuit voltage of 0.729 V, a fill factor of 71.7%, and a short-circuit current density of 21.83 mA/cm^2. The net hole concentration for $CuInS_2$ has been reported to range between 10^{17} and 10^{18} cm^{-3} [29], and tunneling mechanisms due to high carrier density limit the open-circuit voltage [29].

As an effort to improve open-circuit voltage, I. Hengel *et al.* have observed $CuInS_2$ cells by the addition of Ga content and increased open-circuit voltage up to 0.83 V with 11.8% active area efficiency for a $ZnO/CdS/CuInS_2$:Ga cell structure [31]. Some of works were also studied on $CuInS_2$ absorbers by ZnSe [32], Zn(Se,O) [33], and Zn(Se,OH) [34] buffer layers. These works indicate that there are needs for further research on $CuInS_2$ materials to provide an alternative top cell with a potential for high efficiency in tandem systems, even though $CuInS_2$ cell has lower efficiency than CIS and CIGS solar cells. To obtain high-efficiency $CuInS_2$ solar cells, it is crucial to find the optimal composition and grain sizes and more understanding of the intrinsic and extrinsic defects and impurities with the optical and electrical properties of the materials for high quality absorbers.

2.5.2 $CuGa(S_x,Se_{1-x})_2$ Top Cell

The $CuGa(S_x,Se_{1-x})_2$ systems are also suggested for the wide band-gap top cell in tandem structures since their direct band gaps extend from 1.68 eV for $CuGaSe_2$ ($x = 0$) to 2.4 eV for $CuGaS_2$ ($x = 1$) with S contents at room temperature [35]. The lattice parameters (a_o) are 5.614 Å for $CuGaSe_2$ [36] and 5.350 Å for $CuGaS_2$ [37], which lead the utilization of tandem structures with band gap variations. Experimental and theoretical works for these alloys have been reported to gain better understanding of electronic, electrical, and optical properties [38,39]. The growth of epitaxial layers of these materials with crystalline quality has been reported on GaP and GaAs substrates by metalorganic vapor phase epitaxy (MOVPE) [40]. From calculations, the optimum band gap founded for the top cell in the tandem system is 1.72 ± 0.02 eV for a series-connected two-junction tandem solar cell [8]. Therefore, $CuGa(S_x,Se_{1-x})_2$ offers proper band gap ranges for the top cell. No works have been reported on the fabrication of solar cells with these alloys so far. Further research is needed for this alloy system.

2.6 Alternative Buffer Layers for Wide Band-gap $CuGaSe_2$ Top Cell

The $Cd_{1-x}Zn_xS$ (CdZnS) buffer layers give the best lattice matching to the $Cu(In_{1-x},Ga_x)Se_2$ absorber layers. Its band gap is larger than that of CdS buffer layer. Therefore, it leads to the increase in quantum efficiency (QE) at the short wavelength region and a zero-band offset at the $Cd_{1-x}Zn_xS$ and $Cu(In_{1-x},Ga_x)Se_2$ interface. In particular, to provide a favorable conduction band offset for wide band-gap CGS absorbers described above, CdZnS, ZnSe, and Zn(Se,OH) alternative buffer layers are discussed in this section.

Chapters 7 and 8 investigate the device performance of the CIGS and CGS solar cells fabricated with CdZnS buffer layers.

2.6.1 $Cd_{1-x}Zn_xS$ Buffer Layers

In order to obtain a maximum built-in potential, the electron affinities of the absorber and buffer layers should match, and consequently it yields an increased V_{oc} in a solar cell. Due to larger electron affinity of CdS (4.5 eV) than CGS (3.9 eV), a loss in current can occur in the cell. A ternary compound $Cd_{1-x}Zn_xS$, where the electron affinity is varied from 3.7 eV to 4.5 eV, can be used as a buffer layer for a CGS solar cell to minimize a current loss and maximize the V_{oc} of the cell. In addition, by increasing Zn in $Cd_{1-x}Zn_xS$ the lattice parameter (a_o) decreases from 5.82 Å for CdS to 5.42 Å for ZnS, allowing a lattice match to CGS (5.61 Å) or CIS (5.78 Å) and CIGS. The increase in V_{oc} with adding Zn in CdS buffer layer is engaged in the decreased conduction band discontinuity at the junction and the improved built-in voltage.

Investigations of p-type CIS thin films revealed type inversion at the surface [41]. With increasing Ga content in $Cu(In_{1-x},Ga_x)Se_2$ the offset of the conduction bands at the heterojunction changes from a small spike for the CIS to a cliff for the CGS with CdS buffer layer as shown in Figure 2-4. As shown in this figure, mostly, conduction band offset is changed as the Ga content of absorber increases. A negative $\Delta\chi$ ($\chi_n < \chi_p$) produces a conduction band "spike". If $\Delta\chi$ is positive ($\chi_n > \chi_p$), the open-circuit voltage obtainable is reduced. This reduces the usefulness of the cells in tandem structure. The CdS/CGS band alignment increases junction related recombination mechanism, giving a loss in the open-circuit voltage. The existence of a cliff reduces the barrier for recombination at the interface. A spike in the conduction ($\Delta E_c > 0$) is favorable for solar cell efficiency, while a cliff ($\Delta E_c < 0$) limits the open-circuit voltage because of large interface recombination [42].

Therefore, in order to reduce conduction band discontinuity in the CdS/CGS cell structure, a high Zn content in $Cd_{1-x}Zn_xS$ films is essential. However, the $Cd_{1-x}Zn_xS$ films with high Zn content have shown a relatively high resistivity [43]. Furthermore, the carrier density, which increases photocurrent, decreased with increasing Zn [43].

2.6.2 ZnSe Buffer Layers

One of the possible buffer layers for a wide band gap CGS solar cell is ZnSe. Chemical bath deposition (CBD) ZnSe film is a potential candidate to replace toxic CdS on CIGS-based thin film solar cells. ZnSe is a wide band gap material with band gap energy of 2.7 eV [22]. The lattice constants of ZnSe (a_o = 5.668 Å) and CGS (a_o = 5.614 Å) match very well, which results in an almost strain-free interface, compared to the lattice mismatch between CGS and CdS (≈ 4.2%). Measured conduction band offsets for single crystals CdS/CGS and ZnSe/CGS are −0.19 eV and +0.40 eV, respectively [2]. The valence band offsets for CdS/CGS and ZnSe/CGS are also observed 0.8 eV and 0.6 eV, respectively [22]. This ZnSe/CGS structure gives type-I band alignment to form a favorable conduction band spike at the surface with CGS, avoiding a cliff in the conduction band as described above. Therefore, ZnSe is expected to provide a good buffer layer for CGS absorber layer.

CGS solar cells using a ZnSe buffer layer grown by MOVPE have been reported by S. Siebentritt *et al.*, obtaining a 3.3% conversion efficiency [23]. In order to increase solar cell efficiency, further investigations of deposition methods for ZnSe buffer layers and physical processes in the cell structure are required. CGS absorbers by several deposition methods were grown onto the surface of ZnSe single crystals by M. Rusu *et* *al.*, obtaining high open-circuit voltages of 0.85-1.12 V [24]. For the ZnO/ZnSe/Cu(In,Ga)(S,Se)$_2$ solar cell structure, a conversion efficiency of 13.7% was obtained [25].

2.6.3 Zn(Se,OH) Buffer Layers

The best results as buffer layer for CGS solar cells come from chemical bath deposited CdS so far. However, environmental concerns about Cd toxicity in addition to the improvement of cell efficiencies have motivated alternative buffer layers. Buffer layers such as Zn(Se,OH) or Zn(S,OH) deposited by chemical bath are promising materials and have reached an efficiency up to 15% [44]. Zn(Se,OH) has a high band gap value of 2.9 eV [45]. A lattice plane spacing of d_{111} = 3.2 Å was reported [46]. This value corresponds to the cubic structure of ZnSe [46]. From ZnSe/CGS band offset studies an expected band alignment for Zn(Se,OH)/CGS is similar as ZnSe/CGS. This indicates that Zn(Se,OH) buffer layer deposited by a chemical bath process might be a possible candidate for CGS solar cells. CuInS$_2$ solar cells with Zn(Se,OH) buffer layers have also been studied [34]. The works on the solar cells with ZnO/Zn(Se,OH)/Cu(In,Ga)(S,Se)$_2$ structures have shown a 15.7% active area efficiency [44].

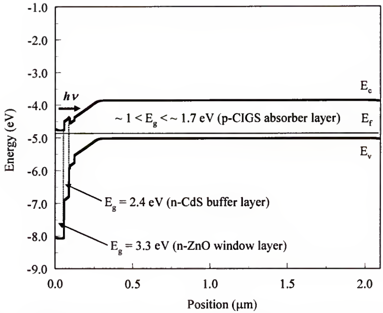

Figure 2-1. Conduction and valence band diagram for a p-n heterojunction ZnO/CdS/CIGS solar cell.

Table 2-1. The performance parameters of the best CIS-based solar cells.

Absorber	V_{oc} (V)	J_{sc} (mA/cm^2)	FF (%)	η (%) (total area)
$CuInSe_2$	0.491	40.58	75.15	15.0
$CuInGaSe_2$	0.692	35.22	79.87	19.5
$CuGaSe_2$	0.823	18.61	66.77	10.2

[1]

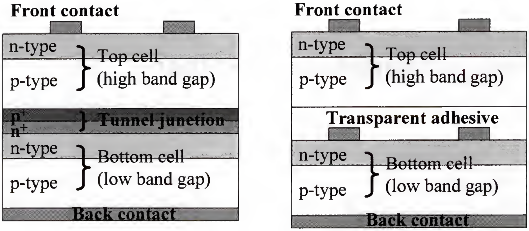

Monolithic structure Mechanically-stacked structure

Figure 2-2. Two-junction monolithically-cascaded and mechanically-stacked tandem solar cell structures.

Table 2-2. The performance parameters of CIS-based thin-film tandem solar cells.

Tandem solar cell structure	V_{oc} (V)	J_{sc} (mA/cm^2)	FF (%)	η (%)
Top: ZnO/CdS/CGS/SnO_2/glass	0.864	15.36	51.25	6.8
Bottom: ZnO/CdS/CIS/Mo/glass	0.456	12.46	69.17	3.9
Mechanically-stacked, four-terminal: CGS/CIS	1.29			9.7
Monolithic: ZnO/CdS/CGS/ITO/n^+Si/pSi/Al	1.32	9.0	43.0	5.1
Monolithic: ZnO/ITO/CdS/CIGS/ZnO/CdS/CIS/Mo/glass	0.688	10.4	52.8	3.8

[47]

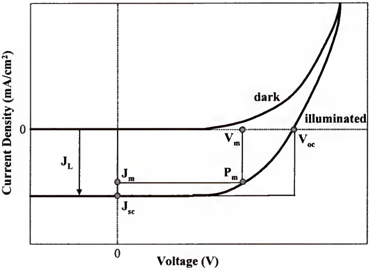

Figure 2-3. Current-density voltage (J-V) characteristics of a solar cell in the dark and illuminated, defining the fundamental solar cell performance parameters: light-generated current density (J_L), short-circuit current density (J_{sc}), and open-circuit voltage (V_{oc}). Fill factor (FF) is determined by the maximum rectangle given by J_m and V_m.

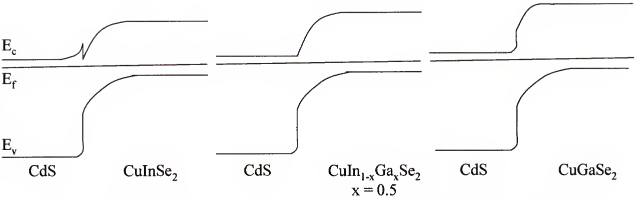

Figure 2-4. Band diagrams with increasing Ga content of the $CuIn_{1-x}Ga_xSe_2$ absorber layer.

CHAPTER 3
DEVICE MODELING AND SIMULATION OF CIGS AND CGS SOLAR CELLS

3.1 Introduction

Much information is available in the literature regarding single-junction $Cu(In_{1-x},Ga_x)Se_2$ (CIGS) solar cells. Increasing the open-circuit voltage (V_{oc}) to improve the overall performance of CIGS cells is highly desirable because it minimizes the interconnection losses in the manufacture of cell modules. Adding gallium (Ga) in the $CuInSe_2$ (CIS) to form CIGS thin films will increase the band-gap energy of the CIGS absorber layer. The CIGS absorber layers can provide a better match to the solar spectrum with increasing the value of V_{oc} and a slight reduction of the short-circuit current density (J_{sc}) in the fabricated CIGS cells. Introducing a spatial variation of the Ga content within the CIGS layer, the band-gap profile can be optimized to increase the photon absorption and carrier diffusion. Furthermore, the Ga profile can be adjusted to optimize the CIGS absorber band-gap profile, and hence improve the V_{oc} and J_{sc} values. Thus, band-gap engineering geared to controlling the spatial distribution of the Ga content in the absorber layer can lead to enhancing the overall performance of CIGS cells.

In contrast to the case of CIGS cells, although $CuGaSe_2$ (CGS) was investigated for several decades, CGS thin film solar cells have not yet achieved as high efficiency as CIGS cells. An n- type inversion layer at the surface of p-type CIGS absorber has been identified for the ZnO/CdS/CIGS heterostructure [48,49]. The n-type type inversion layer formed at the interface decreases available holes at the interface, and hence decreases recombination at the interface. Therefore, recombination in the space charge region is the dominant loss in the high efficiency CIGS solar cells [50,51]. In contrast, the ZnO/CdS/CGS heterostructure does not show an n-type inversion layer at the surface of p-type CGS absorber. Therefore, it was assumed that recombination prevails at the CdS/CGS interface [52].

This chapter presents the device modeling and numerical simulations of CIGS and CGS solar cells. Computer simulations are conducted to analyze the performance of CIGS and CGS cells. The physical model consists of a CIGS cell with a double graded band-gap profile in the space charge region and in the backside of the absorber layer and a uniform band-gap CGS cell. The CIGS and CGS cells described above will be used as a bottom cell and a top cell, respectively, for modeling and numerical simulation of a CGS/CIGS tandem cell structure, as will be depicted in Chapter 4. Furthermore, the performance parameters of the simulation results of the CIGS and CGS cells are compared to the reported experimental data.

3.2 AMPS-1D Device Simulation Program

AMPS-1D (Analysis of Microelectronic and Photonic Structures) is a one-dimensional device simulation program for analyzing and designing transport in device structures [53,54]. This device simulation tool numerically solves the three governing semiconductor device equations such as Poisson's equation and the electron- and hole-continuity equations, and the boundary conditions such as recombination and thermionic emission. Input parameters for AMPS-1D simulation are categorized into three types as follows:

- Parameters for the entire device, including front and back contacts, and temperature.
- Material parameters for each layer, including grid spacing.

- Parameters for illuminating spectrum.

The AMPS can model the solar cells in two different modes: one is the density of state (DOS) mode and another is the lifetime mode. The lifetime mode obtains input parameters as carrier lifetimes form, which is not depending on light and voltage bias, and does not engage in recombination processes. The DOS mode gives the definition of multiple defect states, utilizing defect densities, defect level distributions, and capture cross-sections. Recombination current and defect occupancy are calculated using the Shockley-Read-Hall model based on defect information. Modeling studies for this work used the DOS model. In order to successfully simulate a device, the material parameters for each layer are crucial. However, obtaining the correct material parameter values can be very difficult for those less understood materials. Therefore, the input parameters for defined device structures in this Chapter were chosen from as much as available experimental data, literature values, and reasonably estimated values.

3.3 Modeling and Simulation of CIGS Cells

3.3.1 Cell Structure and Material Parameters

The schematic energy-band diagram under equilibrium condition for a typical ZnO/CdS/CIGS solar cell with a uniform band-gap profile is illustrated in Figure 3-1. CIGS bottom cell structure used in this simulation consists of the layer set: *n*-ZnO, *n*-CdS, high-recombination interface, inverted (*n*) surface, graded (*p*) CIGS absorber modeled as stacked layers, each with a different composition. The layers for the CIGS cell structure are simplified as described above because of uncertainties in the interface and junction and limited material parameters accessible in each layer.

A thin Indium (In) rich *n*-type layer, which is considered to be beneficial to the performance of CIGS cells, exits at the surface of as-grown CIGS film and has been reported by Schmid *et al.* [41]. In the simulation, a 30 nm n- type inverted surface layer is inserted between the n- CdS and p- CIGS layers, and an interface layer with a high density of effective recombination centers is placed at the metallurgical junction between the CdS and inverted surface layers. As an effective recombination center, a deep-level defect is placed in the middle of band-gap of ZnO and CdS layers, high-recombination interface layer, inverted surface layer, and space charge region (SCR) of the CIGS absorber layer. The total thickness of the CIGS absorber layer is maintained at 2 μm. The CIGS absorber layer is divided into the SCR and bulk region in the cell structure. Defect density in the CIGS bulk region is kept around 10^{15} cm^{-3}. Key material parameters for the simulation that differ in each layer are listed in Table 3-1.

3.3.2 The Effect of CdS Layer Thickness on the CIS Cell Performance

Figure 3-2 illustrates simulation results of the effect of CdS buffer layer thickness on the performance of CIS cells. By increasing the CdS buffer layer thickness, values of J_{sc} and FF of the cell decrease. A thick buffer layer causes a poor fill factor as shown in Figure 3-2 (c). The absorption of incident light in the buffer layer increases by increasing the buffer layer thickness, resulting in the decrease of J_{sc}. Moreover, a thicker buffer layer can create a high series resistance in the cell resulting in poor fill factor. In general, very thin CdS films (≤ 50 nm) are commonly used in CIS solar cells. Since light absorbed in the CdS layer usually does not contribute much to the collection of photocurrent, it is desirable that this layer is kept at the minimum thickness possible. The minimum thickness should allow for the CdS conformal coverage of the substrate without the formation of defects that could shunt the cell.

3.3.3 The Effect of Uniform Absorber Band-gap on the Cell Performance

A simulation study of uniform band-gap CIS and CIGS cells was carried out to establish a baseline for comparison. Four representative band-gaps, namely 1.04 eV for CIS and 1.10, 1.18, and 1.22 eV for CIGS, are considered. The simulation results are illustrated in Figure 3-3, showing (a) open-circuit voltage (V_{oc}), (b) short-circuit current density (J_{sc}), (c) fill factor (FF), and (d) efficiency. The simulations were carried out under AM1.5G condition. It is noted that by increasing the CIGS absorber band gap, the value of V_{oc} increases, while the value of J_{sc} decreases as shown in Figure 3-3 (a) and (b). The CIGS cells with higher band gaps have a higher V_{oc} and a smaller J_{sc} than the CIS cells with $x = 0$ and $E_g = 1.04$ eV. The FF values for the cells shown in Figure 3-3 (c) also increase with lager absorber band gaps. The value of efficiency in Figure 3-3 (d) increases from ~ 13% for CIS to a maximum value of ~ 16% at $E_g = 1.22$ eV. CIGS cells with higher Ga-content x = [Ga] / ([Ga] + [In]) of uniform band-gaps were not analyzed because it has been reported in the literature that the device performance degraded when the Ga content in the $Cu(In_{1-x},Ga_x)Se_2$ films exceeds 30 - 40%, *i.e.*, when $x > 0.3 - 0.4$ [55].

3.3.4 The Graded Band-gap Structure of CIGS Cells

The recombination rate in the SCR controls V_{oc} of CIGS cell and can be reduced by increasing barrier height through increasing band-gap in the SCR, and this improves V_{oc} even though a small loss of J_{sc} might be expected if the wider band-gap region is not sufficiently thin [56]. Figure 3-4 illustrates the schematic energy band diagram under equilibrium condition with a double band-gap grading. In this figure, a quasi-electrical field can be established by band-gap gradient incorporating with a high Ga content in the back region of CIGS absorber [57]. It reduces back surface recombination and increases an effective minority-carrier diffusion length. Therefore, it results in an efficient carrier collection, and hence improves both V_{oc} and J_{sc} in CIGS cell. The simulations study by Huang *et al.* revealed that a proper band-gap grading in the SCR and in the back region of CIGS absorber are capable of significantly improving the performance of CIGS cells [58], showing almost 3% higher efficiency than the uniform band-gap CIGS cell.

To provide a high-performance bottom cell in the CGS/CIGS tandem structure, a double band-gap grading is formed in the CIGS absorber by the back surface field (BSF) grading, in which band-gap is linearly increased towards backside, and the SCR grading, in which wider band-gap layer is placed in the SCR, as illustrated in Table 3-2 and also shown in Figure 3-4. The double graded band-gap structure of case 1 in Table 3-2 realizes a high conversion efficiency of 18.39% AM1.5G. Case 2 in Table 3-2 is analogous to case 1, except that the doping density in the CdS layer is increased to 6×10^{17} cm^{-3} and the deep-level defect densities are assumed to be equal to zero in the CIGS absorber. The result yields a maximum conversion efficiency of 19.83% for this cell. This 19.83% CIGS cell described above will contribute as a bottom cell in a stacked CGS/CIGS tandem structure.

3.3.5 Comparison with Experimental Data for CIGS Cells

To test the validity of device modeling, attempts were made to compare the simulation results with reported experimental data for the CIGS cells. The measured values are taken from the photo-current density-voltage (J-V) and normalized quantum efficiency (QE) curves of an experimental CIGS cell with 18.8% efficiency under standard conditions produced at the National Renewable Energy Laboratory (NREL) [59,60]. The performance of this experimental cell is compared with the simulated results of cases 1 and 2 in Table 3-2, and the results are shown in Figures 3-5 and 3-6, where the solid line represents the simulated cell of case 1, the dashed line represents the simulated cell of case 2, and the solid circles denote the experimental values.

Figure 3-5 shows that the photo-J-V curve for case 1 closely matches the experimental curve for the NREL CIGS cell. The photo-J-V values obtained from the simulation of case 2 suggest that a higher efficiency is possible. Figure 3-6 shows a comparison of the simulated QE curve for case 1 with the experimental curve. Excellent agreement was also obtained for this case in the wavelength (λ) range of $0.5\ \mu m \leq \lambda \leq 1.2\ \mu m$.

A separate analysis was carried out to fit the performance of the simulated parameters with data available in the published literature for CIGS cells. Dullweber *et al.* have reported experimental results for band-gap grading in CIGS cells [56,61]. The band-gap structure of the CIGS absorber layer shown in Table 3-3 is based on the Auger depth profile reported by Dullweber *et al.* [56], which allows defining the layer dimensions and compositions for the simulation model. For the simulation study, the depth profile is represented by an equivalent band-gap profile in the CIGS absorber using the equation E_g (y) [eV] = 1.02 + 0.67 y + 0.11 y (y-1) proposed in reference [62], where the variable y denotes the ratio of [Ga]/([Ga]+[In]). The resulting band-gap profile reveals a double-graded CIGS absorber layer with linearly graded band-gap structures in the SCR and in the CIGS bulk layers, as shown in Table 3-3, and was used as a set of input parameters for the simulation study. The notch structure is a particular case of double grading. Theoretical analysis and simulation studies of this structure have been reported [63]. The measured data are also taken from the J-V curve given in Dullweber *et al.* [56]. The key parameters used in fitting the simulation results to the experimental values are the defect density in the inverted surface layer, the defect densities of the midgap deep-level in the SCR, and the defect and hole densities in the CIGS absorber. The results are shown in Figure 3-7, where the simulated values are plotted using a solid line, and the experimental values are indicated by the solid circles. Although the simulated FF is slightly higher than the experiment, excellent agreement was obtained in the J-V curve.

Finally, another work by Dullweber *et al.* [61] for CIGS cells with a normal or reverse graded absorber is considered for fitting the simulation results to experimental values. An absorber with normal grading profile is one where the band-gap is increased linearly from the front to the backside in the entire absorber, while the absorber with reverse grading profile is one where the band-gap is decreased linearly from the front to the back. To investigate these linearly graded structures via simulation, the composition depth profiles of the CIGS absorber given in Dullweber *et al.* [61] were used for the calculation of the band-gap profiles for the CIGS absorber. From the represented band-gap profiles, an absorber structure with normal grading is increased linearly from the front band-gap of 1.03 eV to the backside band-gap of 1.22 eV, while an absorber profile with reverse grading is decreased from 1.24 eV to 1.06 eV. Also, a uniform band-gap profile of 1.14 eV is considered. Experimental performance parameters are also extracted from Dullweber *et al.* [61] for the cases of normal, reverse, and uniform grading, and are compared with the simulated results. The major parameters used in fitting the simulated results to the experimental values are as described in the preceding paragraph. The results are shown in Figure 3-8, where the solid circle and triangle denote the simulated values and experimental data, respectively. The x-axis indicates CIGS absorber band-gap profiles consisting of the reverse grading, uniform, and normal grading from left to right. It is noted that from Figure 3-8 (a) V_{oc} is found to decrease from 565 to 509 mV (a change of 56 mV), from the reverse to the normal grading, while the value of J_{sc} increases from 32.5 to 37.5 mA/cm^2 (a change of 5 mA/cm^2) as shown in Figure 3-8 (b). These trends are also found in the experimental values. Excellent agreement was obtained on the performance parameters V_{oc}, J_{sc}, and FF. Even though the values of conversion efficiency η in the simulation are slightly higher than their experimental counterparts, a reasonable fit was nevertheless obtained.

3.4 Modeling and Simulation of CGS Cells

3.4.1 Cell Structure and Material Parameters

CGS top cell structure considered in this simulation consists of the following material layers: *n*-ZnO, *n*-CdS, interface, uniform *p*-CGS absorber. The CGS cell is limited to a simplified structure described above due to few studies of the material parameters for the CGS absorber and each layer and unknown properties of interface and junction. The CGS absorber layer has a uniform band-gap of E_g (eV) = 1.68 with total thickness kept at 2 μm. In contrast to CIGS cell, it is noted that no inversion layer is presented at the interface between the CdS and CGS layers, as reported by Jasenek *et al.* [21]. In our model, it is assumed that the majority of carrier recombination in CGS cell takes place at the CdS/CGS interface. However, this assumption has not been verified experimentally.

Figure 3-9 shows the energy band diagram of the ZnO/CdS/CGS cell structure. In this diagram, it is noted that no inversion layer is presented at the interface between the CdS and CGS layers. In order to model a recombination center, a deep-level defect is placed in the middle of band-gap of the thin interfacial layer between the CdS and CGS layers. A deep-level recombination center is also placed in the SCR of the CGS absorber. The majority of material parameters for the CGS cell used in the simulation are maintained the same as used for the CIGS cell except the parameters described below.

For the CGS absorber layer μ_n (cm^2/V.s) = 400, μ_p (cm^2/Vs) = 40, carrier density (cm^{-3}) = 10^{17}, χ (eV) = 3.56, and reported experimental values of absorption coefficients [64] and defects [65] are used. Defect density in the CGS bulk region is kept low in the range of $10^{13} \sim 10^{14}$ cm^{-3}. Simulation results on this CGS cell structure yield the performance parameters of η_c = 16.65% AM1.5G, V_{oc} = 1.007 V, J_{sc} = 19.13 mA/cm^2, and FF = 86.4%. The simulated CGS cell described above is used as the top cell in a stacked CGS/CIGS tandem structure.

3.4.2 Comparison with Experimental Data for CGS Cells

The CGS structure cited above was used for fitting the simulation results with the experimental photo-J-V data published in the literature. The experimental photo-J-V data under AM1.5G (100 mW/cm^2) condition were extracted from reference [66] for the ZnO/CdS/CGS cell with a single crystal CGS absorber to compare with the simulated results. This experimental CGS solar cell produces the performance parameters of J_{sc} = 15.5 mA/cm^2, V_{oc} = 0.946 V, FF = 66.5%, and η_c = 9.7%. In the simulation, the thickness in each layer of the cell, defect densities at the interfacial layer and in the CGS absorber layer, the charge densities in the SCR, and capture cross sections for the defects in each layer were used as adjustable parameters to fit the experimental data. The results are shown in Figure 3-10, where the experimental data are plotted in solid lines, and the simulated values are shown by solid circles. From Figure 3-10, it is noted that excellent agreement between the simulation results and the experimental data was obtained for the photo-J-V curve.

3.5 Summary and Conclusions

Device modeling and numerical simulation studies for single-junction CIGS and CGS solar cells have been carried out using the AMPS-1D device simulation program. It is shown that a double band-gap grading using a wide band-gap layer in the SCR and a back surface grading using the gradient of Ga content in the CIGS absorber layer presents an optimal absorber band gap profile to achieve a high-performance CIGS bottom cell with a conversion efficiency of 19.83% AM1.5G. Assuming low defect densities in the CGS absorber and at the CdS/CGS interface, a high-efficiency CGS top cell is obtained for the CGS/CIGS tandem cell structure. Additionally, a comparison of the simulation results with the reported experimental data shows good agreement in the photo-J-V and QE curves between the theoretical calculations and the experimental data for the CIGS and CGS cells.

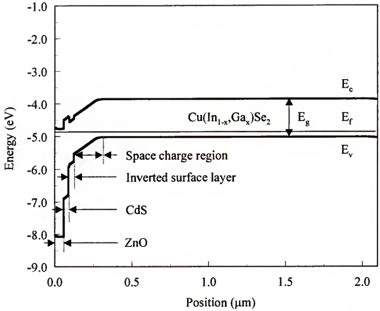

Figure 3-1. The schematic energy-band diagram of a typical ZnO/CdS/CIGS solar cell under equilibrium condition.

Table 3-1. Material parameters of CIGS bottom cell.

Layer parameters	ZnO	CdS	Inverted surface	Graded CIGS absorber
Thickness (nm)	50	30	30	2000
Band gap E_g (eV)	3.3	2.4	1.3	1.16-1.4 (varied)
Electron affinity χ (eV)	4.0	3.75	3.95	3.75-3.87 (varied)
Electron mobility μ_n (cm^2/Vs)	50	6	10	300
Hole mobility μ_p (cm^2/Vs)	5	3	5	30
Type	N	N	N	P
Carrier density (cm^{-3})	5×10^{17}	6×10^{16}	10^{12}	8×10^{16}
Dielectric constant	9	10	13.6	13.6
Effective density N_c (cm^{-3})	10^{19}	10^{19}	3×10^{18}	3×10^{18}
Effective density N_v (cm^{-3})	10^{19}	10^{19}	1.5×10^{19}	1.5×10^{19}

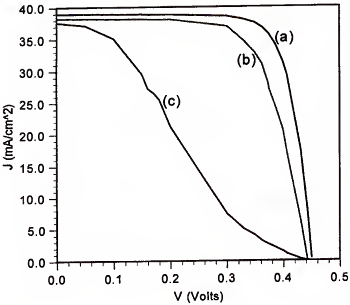

Figure 3-2. The photo-J-V curves for the simulated CIS cells with different thickness of CdS buffer layer for (a) 30 nm, (b) 60 nm, and (c) 80 nm.

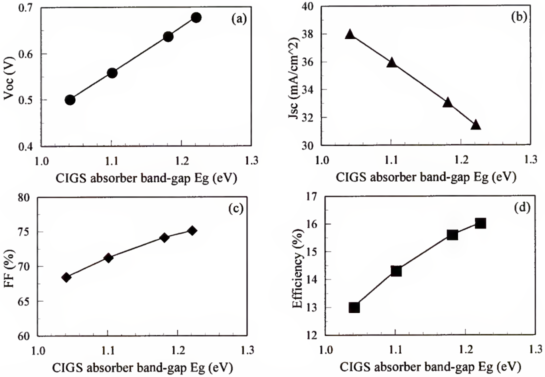

Figure 3-3. Simulated performance parameters of the CuInSe$_2$ (E$_g$ = 1.04 eV) and Cu(In$_{1-x}$,Ga$_x$)Se$_2$ (E$_g$ = 1.10, 1.18, and 1.22 eV) cells with different uniform absorber band-gap profiles; (a) V$_{oc}$, (b) J$_{sc}$, (c) FF, and (d) efficiency.

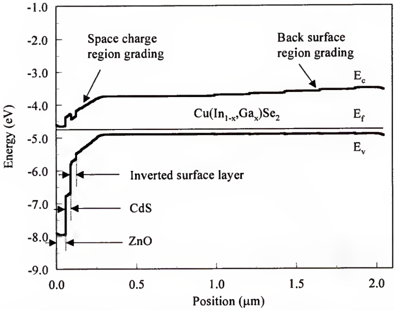

Figure 3-4. The schematic energy-band diagram of a CIGS cell with a double band-gap grading profile under equilibrium condition.

Table 3-2. Simulated performance parameters of the CIGS solar cells with a double band-gap grading profile.

	Band-gap profile	η_c (%)	V_{oc} (mV)	J_{sc} (mA/cm^2)	FF (%)
Case 1	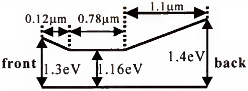 1.1μm 0.12μm 0.78μm front 1.3eV 1.16eV 1.4eV back	18.39	675	34.31	79.4
Case 2	Same profile as case 1	19.83	688	34.42	83.8

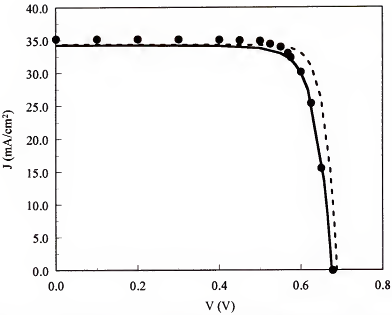

Figure 3-5. The photo-J-V curves for the simulated results (solid and dashed lines) and the reported experimental data (solid circles) [59,60].

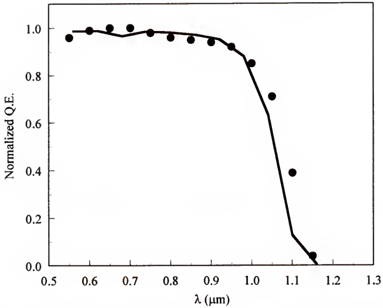

Figure 3-6. The normalized QE for the simulated results (solid line) and the reported experimental data (solid circles) [59].

Table 3-3. The energy band-gap profile of the CIGS absorber layer used in simulation.

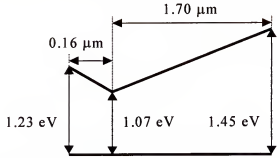

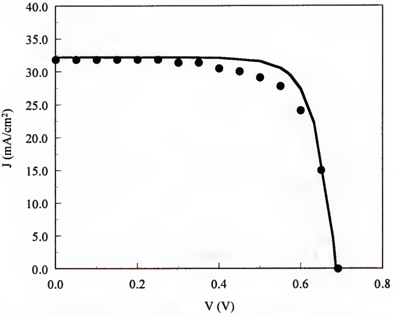

Figure 3-7. The photo-J-V curves for the simulated results (solid line) and the published data (solid circles) [56].

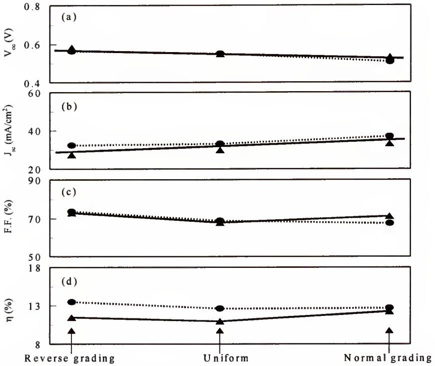

Figure 3-8. A comparison of the performance parameters for the simulated results (circles) and the published data (triangles) [61].

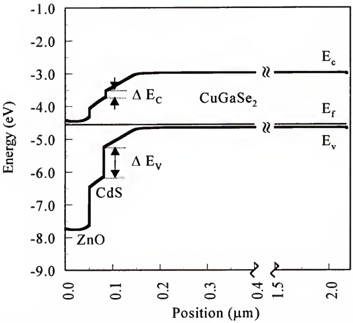

Figure 3-9. The schematic energy-band diagram for a CGS cell under equilibrium condition.

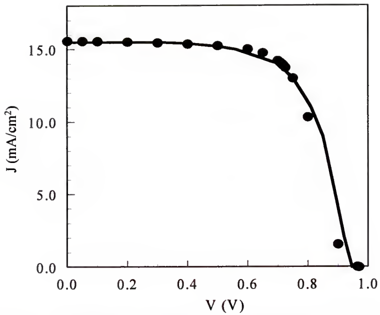

Figure 3-10. The photo-J-V curve for the simulated results and the published data [66].

CHAPTER 4
NUMERICAL SIMULATION OF MECHANICALLY-STACKED CGS/CIGS TANDEM SOLAR CELLS

4.1 Introduction

Tandem solar cells can be formed by either mechanically stacked or monolithically cascaded solar cells [67,68]. A two-junction four-terminal mechanically-stacked tandem cell can be attained by the top and bottom cells fabricated individually and bonded together. In contrast, a two-junction two-terminal monolithically-cascaded tandem cell consists of a top cell grown on top of a bottom cell with an optically transparent tunnel junction that electrically connects the top and bottom cells.

Mechanically stacked tandem cells allow independent operation of stacked cells while monolithically cascaded cells require a current matching between the top and bottom cells and a high-quality tunnel junction. The optimal band gap energies for a two-junction tandem cell is in the range of 1.6 to 1.8 eV for the top cell, and 0.9 to 1.2 eV for the bottom cell [5-7].

The combination of $CuGaSe_2$ (CGS) with a band gap of 1.68 eV and $CuInSe_2$ (CIS) with a band gap of 1.04 eV could provide an excellent tandem cell configuration. A conversion efficiency of 33.9% at AM 1.5 global spectrum was theoretically predicted for a CGS/CIS tandem cell [17]. A mechanically stacked, series connected four-terminal CGS/CIS tandem cell has been fabricated and achieved an efficiency of 9.7% at AM1.5G [47].

A graded $CuIn_{1-x}Ga_xSe_2$ (CIGS) absorber, formed by adding Ga to CIS film, is realized by varying x through the depth of the film. Such a grading profile corresponds to create a grading of band gap, with band-gap energies varying between 1.04 eV (CIS) and 1.68 eV (CGS). High performance of top and bottom cells is necessary to give maximum overall tandem efficiency. Therefore, a CIGS cell with graded band-gap structure in the absorber layer can serve as a high-quality bottom cell for a tandem configuration. Since a top cell makes a large contribution to overall tandem efficiency, this requires a high-quality top cell.

In this chapter, device modeling and numerical computer simulation are conducted on the performance parameters of a four-terminal mechanically-stacked CGS/CIGS tandem cell. A CIGS cell with graded CIGS absorber and a CGS cell with uniform CGS absorber are used as bottom and top cells, respectively, as presented in Chapter 3. The investigation focuses on the study of the effect of varying top-cell absorber thickness on the bottom-cell performance. The CGS/CIGS tandem-cell efficiency is also investigated as a function of the absorber thickness of top cell.

4.2 Mechanically-Stacked CGS/CIGS Tandem Cell Structure

A mechanically stacked tandem cell is modeled with a top cell mounted on top of a bottom cell. A poor top cell combined with a superior bottom cell could produce a low-performance tandem cell. Therefore, high-performance top and optimized bottom cells are required to obtain maximum overall cell efficiency. A CGS cell with uniform band gap in the CGS absorber region is used as a top cell for a tandem structure. A CIGS cell with double graded band gap in the CIGS absorber region is used as a bottom cell for a tandem structure. The two cells are connected externally to form a four-terminal device. This approach allows fabrication of individual cells that operate independently. Thus, photocurrents in the two cells do not have to be matched in the four-terminal configuration. Figure 4-1 shows a schematic of a four-terminal mechanically stacked CGS/CIGS tandem cell structure for simulation.

4.3 Simulation Method

The computer device simulation program AMPS-1D is utilized to model a cell structure by inputting material parameters in each specified layer. The CGS and CIGS cells are modeled and simulated separately under AM1.5G illumination with the tandem structure as illustrated in Figure 4-1. The number of photons N_{ph} (x) remaining in the beam after traveling a thickness x of the material is defined by $N_{ph}(x) = N_{ph}(0)\, e^{-\alpha x}$, where N_{ph} (0) is the number of photons at $x = 0$ and α is the absorption coefficient at wavelength, λ. Values of photon flux (#/cm^2-sec) after traveling CGS top cell layers are calculated as a function of CGS absorber layer thickness, and the calculated photon flux at λ is used as the incident flux value for the CIGS bottom cell underneath the top cell in the simulation.

The thickness of the CGS absorber layer is varied from 0.4 to 2 μm, while the thickness of other layers of the CGS top cell remains same in the calculation. The CGS top cell is simulated as a function of the CGS layer thickness, and the CIGS bottom cell underneath the CGS top cell is also simulated depending on the CGS layer thickness of the top cell. The tandem cell efficiency of a mechanically stacked four-terminal structure can be obtained by adding those two efficiencies of the top and bottom cells.

4.4 The Effect of CGS Top Cell Thickness on the Performance of CIGS Bottom Cell

Numerical simulation of the performance of the bottom CIGS cell underneath the top CGS cell, which is stacked mechanically, is carried out under AM1.5G. The thickness of the CGS absorber layer of the top cell is varied from 0.4 to 2 μm. The CGS top cell with a 2 μm CGS layer has produced the performance parameters of η = 16.65%, V_{oc} = 1.007 V, J_{sc} = 19.13 mA/cm^2, and FF = 86.4%, as described in Chapter 3. The performance of the stand-alone CIGS bottom cell with a 2 μm CIGS layer is given by η = 19.83%, V_{oc} = 0.688 V, J_{sc} = 34.42 mA/cm^2, and FF = 83.8%, as described in case 2 of Table 3-2 in Chapter 3.

Stacking two cells described above, the performance characteristics of the bottom cell underneath the top cell are obtained from AMPS-1D simulation as a function of CGS layer thickness, and results are shown in Figure 4-2. The first data point in each Figure shows the performance parameters of the stand-alone CIGS cell. As shown in Figure 4-2 (c), J_{sc} of the CIGS cell is decreased once a top cell exits over a bottom cell. The efficiency that depends on J_{sc} is decreased simultaneously because there are almost no changes for V_{oc} and FF as shown in Figure 4-2 (a), (b), and (d).

Therefore, it is noted that the performance parameters of the CIGS bottom cell, such as values of J_{sc} and η, underneath the CGS top cell with initial CGS absorber thickness of 0.4 μm in a stacked tandem cell drop to almost less than half of those of the stand-alone CIGS bottom cell. It is shown that the values of J_{sc} and η are in the range of $15<J_{sc}<18$ mA/cm^2 and $8<\eta<10$% for further increasing absorber thickness, respectively.

4.5 The Effect of CGS Absorber Thickness on the Performance of CGS/CIGS Tandem Cell

Studies of the CGS/CIGS tandem cell as a function of CGS layer thickness of the top cell are carried out under AM1.5G. A CGS top cell is also simulated as a function of CGS layer thickness up to 2 μm to study the effect of CGS absorber thickness on the performance of the top cell. Furthermore, to see the effect of the thickness of the top cell absorber layer on the performance of the tandem cell, the efficiency of the CGS/CIGS tandem cell is obtained by adding two efficiencies of the CGS top cell and the CIGS bottom cell under the top as a function of CGS absorber thickness. The results are shown in Figure 4-3. The bottom solid line with data points of Figure 4-3 indicates efficiency of the CIGS bottom cell underneath the CGS top cell as a function of CGS layer thickness, while the line in the middle represents that of the CGS top cell. The line in the top indicates composite efficiency of the CGS/CIGS tandem cell.

A tandem cell efficiency of 25.22% was obtained using a 16.65% top cell and an 8.57% bottom cell underneath the top cell with a 2 μm CGS absorber thickness as shown in Figure 4-4. Individual band gap cell has a different current and voltage output. The performance of series-connected cells is determined by the worst cell in the tandem system. Since the J_{sc} is determined by the J_{sc} of the bad cell, the short-circuit current density of the CGS/CIGS tandem cell shown in Figure 4-4 can approximately be estimated as ~ 15.47 mA/cm^2, while the open-circuit voltage of the tandem cell is 1.675 V which can be obtained by the sum of those of the individual cells. The advantage of the four-terminal structure is that the number of available semiconductor materials is considerably larger and thus gives broad flexibility.

As described in the previous sections, the efficiency of the CIGS bottom cell is decreased dramatically when the top cell is stacked on the bottom cell. Consequently, the CIGS bottom cell has an efficiency in the range of 8 ~ 10% for the entire range of CGS layer thickness. A tandem cell efficiency of 25.22% is obtained by using a 2 μm CGS absorber layer with a CGS top cell efficiency of 16.65% and a CIGS bottom cell efficiency of 8.57%. From the simulation results, it is shown that two-third of the tandem cell efficiency is derived from the top cell. Therefore, it is obvious that a high-performance CGS top cell is a key factor to achieve a high-performance CGS/CIGS tandem cell. Furthermore, our simulation results suggest that it is possible to achieve a 25% AM1.5G conversion efficiency with a high-efficiency CGS top cell (η>16%) and an optimized CIGS bottom cell for the CGS/CIGS two-junction tandem cell.

4.6 Summary and Conclusions

Device modeling and numerical simulation studies on a mechanically stacked CGS/CIGS tandem cell have been carried out using the AMPS-1D device simulation program. A CIGS cell with double graded CIGS absorber and a CGS cell with uniform CGS absorber have been used as the bottom and top cells for the tandem cell structure. It is shown that the performance parameters such as J_{sc} and η of the CIGS bottom cell decrease to less than half compared to that of stand-alone CIGS cell when the CGS top cell is mounted on the CIGS bottom cell. Simulation results of the CGS/CIGS tandem cell show that 25% AM1.5G conversion efficiency could be achieved by using a CGS top cell with $\eta > 16\%$ and an optimized CIGS bottom cell structure.

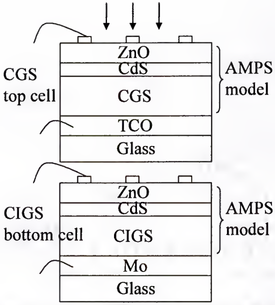

Figure 4-1. A schematic of a four-terminal mechanically-stacked CGS/CIGS tandem cell structure.

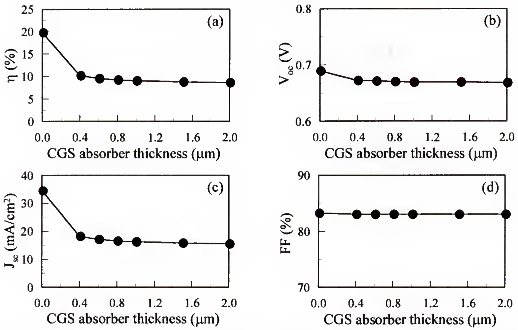

Figure 4-2. Performance parameters of CIGS bottom cell under working CGS top cell as a function of CGS absorber thickness.

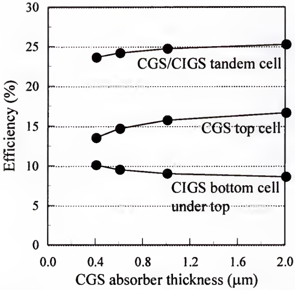

Figure 4-3. Efficiencies of CGS/CIGS tandem cell, CGS top cell, and CIGS bottom cell under top cell as a function of CGS top cell absorber thickness.

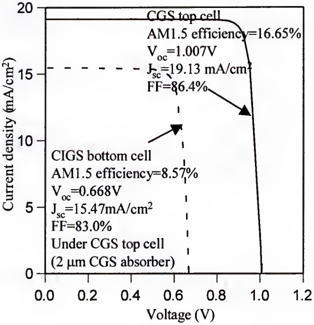

Figure 4-4. Simulated photo-J-V curves of a CGS top cell and a CIGS bottom cell under the CGS top cell for a CGS/CIGS tandem cell with an efficiency of 25.22%.

CHAPTER 5
DEVELOPMENT, GROWTH, AND CHARACTERIZATION OF CHEMICAL-BATH-DEPOSITION CDZNS BUFFER LAYERS

5.1 Introduction

For thin film CIGS-based solar cells, buffer layer materials such as CdS, $Cd_{1-x}Zn_xS$, ZnS, ZnO, $Zn_x(O,S)_y$, $Zn(O,OH)_x$, $Zn(O,S,OH)_x$, ZnSe, Zn(Se,OH), Zn(S,Se), ZnInSe, ZrO_2, $In(OH)_3$, In_2S_3, $In(OH)_xS_y$, SnO_2, or $Sn(S,O)_2$ deposited by chemical bath deposition (CBD) [69-74], atomic layer deposition (ALD) [75], physical vapor deposition (PVD) [76], metal-organic chemical vapor deposition (MOCVD) [77,78], or successive ionic layer absorption and reaction (SILAR) have been investigated [79,80].

In view of environmental safety, it is highly desirable to replace CdS ($E_g \approx 2.4$ eV) by cadmium (Cd) free and toxic-free alternative buffer layers. In addition, wider band-gap buffer materials are preferred for CIGS cells, since they allow transmission of shorter wavelength photons into CIGS absorber and hence higher short-circuit current density (J_{sc}) could be expected. For this purpose, zinc (Zn)-based compound materials such as ZnO ($E_g \approx 3.3$ eV), $Zn_x(O,S)_y$ ($E_g \approx$ between 3.3 and 3.8 eV), $Zn(O,S,OH)_x$, and ZnS ($E_g \approx 3.8$ eV) deposited by CBD process are proposed as alternative buffer layers for CIGS thin film solar cells.

Thin film solar cells using CBD-ZnO/CIGSS, ALD-Zn(O,S)/CIGS, PVD-$Cd_{1-x}Zn_xS$/CIS, CBD-ZnS/CIGS, and CBD-$Zn(O,S,OH)_x$/CIGS have achieved conversion efficiencies of 14.3% [81], 16% [82], 12.3% [83], 18.6% [84], and 14.2% [85], respectively. Compared to the best performance CdS/CIGS solar cells with a total area efficiency of 19.5% AM1.5G [1], these Zn-based buffer layers are very promising for replacing the CdS buffer layer on CIGS cells.

The addition of Zn to the most widely used CdS buffer layer material decreases the lattice constant with a lattice-match to CGS absorber and produces a more favorable conduction band alignment. It has been demonstrated that adding Zn enhances both the open-circuit voltage and short-circuit current of the device to yield higher conversion efficiency for the CGS cells [86]. Increasing Zn concentration in the $Cd_{1-x}Zn_xS$ (CdS: $E_g \approx 2.4$ eV, ZnS: $E_g \approx 3.8$ eV) films increases band-gap energy, which results in an increase in short wavelength photo-response. Therefore, $Cd_{1-x}Zn_xS$ could lead to the increase in quantum efficiency (QE) at shorter wavelengths and a favorable band offset at the interface $Cd_{1-x}Zn_xS$ buffer and the wider band-gap CGS absorber layer.

The CIS solar cells with PVD-$Cd_{1-x}Zn_xS$ (In-doped) buffer have demonstrated an efficiency of up to 12.3% [83] with a 17% Zn-composition. Furthermore, the influence of Zn-composition, x, in the $Cd_{1-x}Zn_xS$ films on the properties of interface layers has not yet fully understood. Therefore, studies of $Cd_{1-x}Zn_xS$ buffer layers to replace the CdS buffer layer for the CIGS and CGS solar cells are desirable.

This chapter presents the development, growth, and characterization of $Cd_{1-x}Zn_xS$ (denoted as CdZnS) films prepared by chemical bath deposition (CBD) for use as buffer layers in CIGS and CGS thin film solar cells.

5.2 Development and Growth of CBD-CdZnS Buffer Layers

5.2.1 Chemical Bath Deposition Technique

The CBD technique involves the controlled precipitation from solution of a compound on a suitable substrate. The technique offers many advantages over CVD, MBE, and spray pyrolysis. Factors such as control of film thickness and deposition rate by varying the solution pH, temperature and reagent concentration are allied with the ability of CBD to coat large areas, in a reproducible and low cost process. In addition, the homogeneity and stoichiometry of the product are maintained partly. A major drawback of the CBD process is the inefficiency of the process, in terms of the utilization of starting materials and their conversion to thin films. The competing homogeneous reaction in solution which results in massive precipitation in solution and deposition of material on the CBD reactor walls limit the extent of the heterogeneous reaction on the substrate surface. However, the technique is simple and requires relatively low capital expenditure, films may be deposited at very low temperatures upon a variety of substrates, the process may be easily adapted to large area processing at low fabrication cost, and the thickness of the deposited layers may be controlled by variation of the length of the deposition time.

5.2.2 Chemical Bath Deposition Condition

The chemicals used in this work consist of aqueous solutions of 1.20×10^{-3} M $CdCl_2\cdot2(1/2)H_2O$, 1.39×10^{-3} M NH_4Cl, 1.19×10^{-2} M thiourea (H_2NCSNH_2), 6.27×10^{-4} M $ZnCl_2$, and 5.27×10^{-4} M NH_3. By varying the relative ratio of Cd and Zn ions, the $Cd_{1-x}Zn_xS$ films with solution composition parameter x_{bath} = 0, 0.3, and 0.5 were deposited on soda-lime-glass (SLG) substrates. The bath temperature of the solution was kept around 85 °C. The deposition time ranged from 20 to 90 minutes according to the mixture ratio in the solution. The value of pH was kept at 7.0 in all sample preparation. SLGs, used as substrates, were cleaned by washing in DI water, detergent, ultrasonic cleaner, and 3 step cascade. The cleaned SLG substrates were submerged into the starting solution vertically for deposition of CdZnS films.

5.2.3 Definition of the Relative Zinc Content in the Buffer Film and in the CBD Solution

The composition of Zn relative to that of Cd in the CBD solution is given by the expression

$$x_{bath} = [Zn] / ([Zn] + [Cd])$$

where [Zn] and [Cd] represent the concentrations of Zn and Cd in the liquid solution. On the other hand, the relative composition of Zn in the solid $Cd_{1-x}Zn_xS$ buffer film is given by the subindex x, where

x = stoichiometric composition of Zn in a solid $Cd_{1-x}Zn_xS$ film

The relationship between x_{bath} and x is also the subject of research. However, for the purposes of reporting results in this chapter and also the subsequent chapters, we make the simplifying assumption that

$$x = x_{bath}$$

Thus, when we refer to a $Cd_{1-x}Zn_xS$ film as having a relative fractional zinc composition x = 0.3, this statement should be interpreted to mean that the film in question was grown using a CBD solution with a concentration characterized by $x_{bath} = 0.3$.

5.3 Characterization of CBD-CdZnS Thin Films

5.3.1 Thickness of CdZnS Films

The film thickness of CdZnS buffer layers was measured using a Tencor profiler. The CdZnS films were deposited on the surface of SLG substrates, and were covered by #1529 photo resist. The system was then baked for 5 minutes at 110 °C, etched by dipping in diluted 10% HCl solution for 20 seconds, rinsed by DI water, and finally cleaned by acetone and isopropyl alcohol.

Figure 5-1 shows the film thickness observed as a function of deposition time for CdZnS films with relative zinc compositions x = 0, 0.3, and 0.5. It is important to point out that all the films shown in Figure 5-1 were obtained through a single CBD process. For example, for x = 0, three SLG substrates were submerged in the CBD solution at the same time, and the glass substrates were removed from the bath, one at a time, after 20 min., 30 min, and 40 min, respectively. The results show that the growth rate of CdZnS films with relative zinc composition x = 0 (CdS) was faster compared to that of CdZnS films with x = 0.3, and also the growth rate of films with x = 0.3 was faster compared to that of films with x = 0.5 as the deposition time grew longer. The deposition rate decreases with increasing relative Zn content in the bath.

Figure 5-2 shows the variation of the thickness of the films for different values of relative zinc composition x at a constant deposition time of 50 minutes. The thickness of the films is found to decrease with an increase of Zn content in the bath. Films showed poor adherence, and colors varied from yellow to mostly white with yellow tints, as the composition x increases up to 0.7. Similar observations have been reported in the literature [71].

5.3.2 Structural Analysis

A powder X-ray diffractometer with Cu Kα radiation was used to investigate the structural properties of CdZnS films deposited on the SLG substrates. The CdZnS films prepared by a single CBD process did not show any peaks due to the very thin nature of the films. Clear diffraction peaks were obtained using thicker films grown by executing three sequential CBD operations, resulting in an approximate thickness of 200 nm (using a bath with relative zinc composition x = 0), 100 nm (x = 0.3), and 150 nm (x = 0.5). The resulting powder XRD patterns for CdZnS films with x = 0, 0.3, and 0.5 are shown in Figure 5-3. A comparison of the 2θ peak-positions of the JCPDS XRD spectra data for the film with x = 0 (*i.e.*, a CdS film) suggests that the as-deposited CdZnS films have hexagonal (wurtzite group) structures with X-ray diffraction peaks corresponding to the (100), (002), (101), (102), (110), (103), (112), and (004) planes. The peaks become weaker for films with Zn composition of x = 0.3, and no peaks were observed for x = 0.5, implying the presence of amorphous structures.

It is difficult to analyze diffractions of thin films due to their low diffracted intensities produced by the film compared to those of the substrate and background. A approach for analyzing thin films is to use Grazing Incidence-Angle X-ray Diffraction (GIXRD), which intensifies the diffracted signal by increasing the path length of the incident X-ray beam by using a very small angle (ω) between the incident beam and the film surface. To investigate the structural properties of CdZnS thin layers near the surface or on the surface itself, we used GIXRD with a grazing angle ω = 0.4 °. Thin films with relative zinc compositions x = 0, 0.3, and 0.5 were deposited by a single CBD process on Mo-coated SLG substrates. The approximate thickness of the resulting films was in the range of 50 ~ 60 nm. The GIXRD patterns for CdZnS films with x = 0, 0.3, and 0.5 are shown in Figure 5-4. It was observed that the 2θ diffraction-angle of the main peaks shifts to a slightly higher angle with increasing relative Zn composition, due to the elemental substitutions of Zn for Cd. It is also found that the peaks of CdZnS thin film with x = 0.5 becomes less pronounced, suggesting a decrease in the crystalline nature of the film at that level of zinc content.

5.3.3 Analysis of Surface Morphology

The surface characteristics of CdZnS films grown on SLG substrates were examined using a field emission scanning electron microscope (SEM). The thickness of the CdZnS films studied lied in the range of 70 to 150 nm. Figures 5-5, 5-6, and 5-7 show the SEM micrographs of the CdZnS films for different values of relative zinc composition x. The film surface shows larger grains as the relative Zn content is increased from x = 0 to x = 0.3. A reduction in crystallinity was observed for the film with x = 0.5. This is also consistent with the evidence found in the powder and grazing incidence XRD patterns, where much sharper peaks are observed for the films with x = 0 and 0.3 compared to the weak peaks observed in the film with x = 0.5.

5.3.4 Optical Analysis

Optical absorbance and transmittance (T) spectra of CdZnS films were measured using an HP 8453 UV-Visible spectrophotometer over the wavelength range of 300 to 1100 nm. Figure 5-8 shows the spectral dependence of the transmittance for the CdZnS films with relative zinc composition x = 0.3 deposited on the SLG substrates. For very thin CdZnS films, better than 80% transmittance was obtained at short and long wavelengths, while the film with a thickness of 80 nm has a 70% transmittance for wavelengths longer than 600 nm. The film with a thickness of 50 nm shows 80% transmittance for wavelengths longer than 600 nm. These values are comparable to those reported elsewhere [87,88].

The thinner films (*i.e.*, those grown with shorter deposition times) have a higher transmittance at shorter wavelengths, which is a desirable feature for enhancing the short-circuit current. On the other hand, thicker films could assist in avoiding damages caused by the subsequent ZnO sputtering deposition process required to build a solar device. Therefore, optimization of the buffer layer thickness is essential for improving the overall cell performance. Figure 5-9 shows the optical transmittance spectra for CdZnS films with relative zinc composition x = 0 (*i.e.*, a CdS film) and relative zinc composition x = 0.3. The spectral behavior of these films shows that the absorption edges shift to shorter wavelengths as the relative Zn content increases from x = 0 to 0.3. As indicated in the figure caption, the film thicknesses used in the study were 200 nm ($x = 0$) and 100 nm ($x = 0.3$).

The absorption coefficient α (cm^{-1}) for the thin film can be obtained from transmission data in the high absorption region through application of the formula

$$\alpha = (1/d) \times ln(1/T)$$

where d (cm) is the thickness of the film, and T is the transmittance of a single-side deposited CdZnS film. Once the absorption coefficient is extracted from the transmission data, for direct transition, the values of the optical bang-gap energy (E_g) of CdZnS films can be estimated using the theoretical relationship

$$\alpha h\nu = \text{constant} \times (h\nu - E_g)^{1/2}$$

where $h\nu$ represents the photon energy. Figure 5-10 shows the resulting plots of the quantity $(\alpha h\nu)^2$ versus photon energies in the range 1.0 - 3.5 eV. Finally, from these plots and the underlying theoretical relationship it is possible to extract the energy band-gap values reported in Table 5-1, which shows that $E_g = 2.4$ eV for $x = 0$ (CdS), $E_g = 2.55$ eV for CdZnS with $x = 0.3$, and $E_g = 2.7$ eV for CdZnS with $x = 0.5$. Therefore, the net effect of including additional Zn content in the buffer later is to increase the energy band gap of the CdZnS films.

5.3.5 Electrical Analysis

The electrical resistivity of the films under study was characterized by the I-V measurements using an Al/CdZnS/ITO "sandwich" structure and an MMR Hall effect and Van der Pauw measurement system.

The I-V measurements yielded the results reported in Table 5-2, which shows the resistance, resistivity, and conductivity of CdZnS thin films as a function of the relative composition x. In order to measure the electrical resistivity of CBD-CdZnS layers, circular aluminum contact dots with a thickness of 100 nm and a diameter of 200 μm were deposited by electron-beam evaporation. Square glass substrates of 1"× 1" in size were coated with 100 nm of indium-tin-oxide (ITO). Prior to the deposition of CdZnS, the substrates were successively cleaned using acetone, methanol, and isopropyl alcohol. The Al/CdZnS/ITO sandwich structure produced good ohmic contacts for the CdZnS films. The electrical resistance (R), electrical resistivity (ρ), and electrical conductivity (σ) were estimated using the as-deposited CdZnS film with thickness of 70 ~ 80 nm and a contact area of 3.14×10^{-4} cm^2. The measured values of R, ρ, and σ are summarized in Table 5-2. The measured electrical resistivities of CdZnS thin films are in the range of 2 ~ 5 $\times10^3$ Ω·cm, and the resistivity is found to increase with increasing Zn composition.

The electrical resistivity was also measured using a four-probe MMR Hall effect and Van der Pauw measurement system. The thickness of the films used in this set of measurements lied in the range of 100 to 200 nm. The results indicate that the resistivities of the as-deposited CdZnS films change from approximately 10^2 to 7×10^3 Ω·cm as the value of relative zinc composition x increases from 0 to 0.5. Theses results show a trend analogous to the resistivity results obtained using the Al/CdZnS/ITO sandwich structure. It was also observed that the carrier density decreased with increasing Zn content. The carriers found in the films are electrons. Similar trends have also been reported elsewhere [43,89].

5.4 Summary and Conclusions

In this chapter, we have demonstrated that CdZnS materials with specific Zn contents have attractive physical properties for use as buffer layer materials for the CIGS and CGS solar cells. In particular, buffer layers of various relative stoichiometric compositions of Zn, denoted by the subindex x in the chemical formula $Cd_{1-x}Zn_xS$, were deposited on the SLG substrates. Their structural, surface morphology, optical, and electrical properties were characterized and analyzed by XRD, SEM, spectrophotometer, and resistivity studies. The experimental studies showed that the film growth rate during the CBD process slows down as the zinc content increases; hence, a longer deposition time is needed for growing a CdZnS film than for growing a CdS film to a given thickness. The experimental results give an estimate of the expected growth rate as a function of the zinc content in the solution. The degree of crystallinity in the film decreased with increasing relative zinc content x, leading to an amorphous structure at the concentration level $x = 0.5$. In addition, the resistivity of the CdZnS films also increased with increasing relative zinc content x. Of particular relevance is also the fact that the energy band gap of CdZnS is higher than that of CdS, and that the band gap increases with increasing zinc content x. One conclusion is that CdZnS films with relative zinc composition $x = 0.3$ showed better than 80% transmittance for wavelengths longer than 600 nm with film thicknesses less than 50 nm. Because of their high transmittance, CdZnS can be useful as a buffer layer for the CGS and CIGS solar cells. Therefore, it is concluded that from the structural, surface, optical, and electrical analyses, the $Cd_{1-x}Zn_xS$ film with relative Zn content $x = 0.3$ is an excellent candidate as buffer-layer material for the CIGS and CGS solar cells.

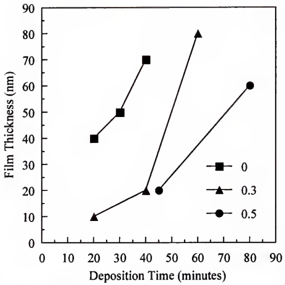

Figure 5-1. Film thickness as a function of deposition time for CdZnS films with relative zinc compositions x = 0, 0.3, and 0.5.

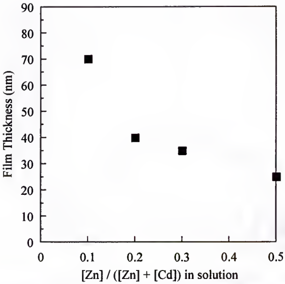

Figure 5-2. Film thickness variation as a function of relative zinc composition x for CdZnS films with deposition time of 50 minutes.

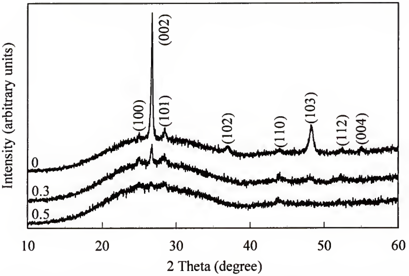

Figure 5-3. Powder XRD patterns of CdZnS films deposited on SLG with relative zinc composition x = 0 (film thickness d ≈ 200 nm), x = 0.3 (d ≈ 100 nm), and x = 0.5 (d ≈ 150 nm).

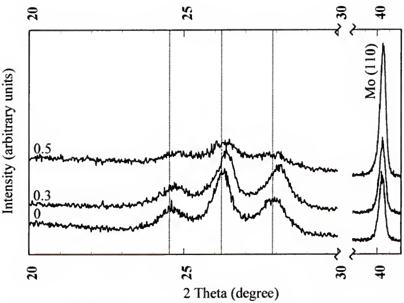

Figure 5-4. Grazing incidence XRD patterns of CdZnS films, deposited on Mo, with relative zinc compositions x = 0, 0.3, and 0.5.

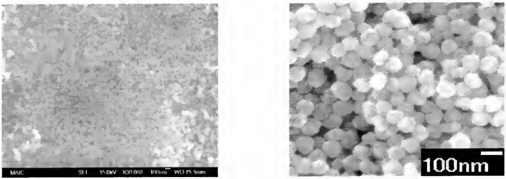

Image 1: Actual magnification: 30,000X
Accelerating voltage: 15 kV

Image 2: Selected region
Actual magnification: 30,000X

Figure 5-5. SEM micrographs of the surface of a $Cd_{1-x}Zn_xS$ thin film with relative zinc composition x = 0 (CdS).

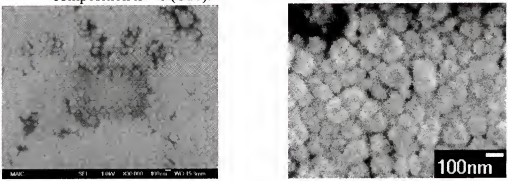

Image 3: Actual magnification: 30,000X
Accelerating voltage: 1 kV

Image 4: Selected region
Actual magnification: 30,000X

Figure 5-6. SEM micrographs of the surface of a $Cd_{1-x}Zn_xS$ thin film with relative zinc composition x = 0.3.

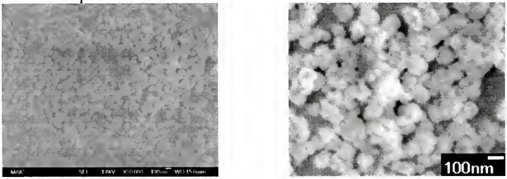

Image 5: Actual magnification: 30,000X
Accelerating voltage: 1 kV

Image 6: Selected region
Actual magnification: 30,000X

Figure 5-7. SEM micrographs of the surface of a $Cd_{1-x}Zn_xS$ thin film with relative zinc composition x = 0.5.

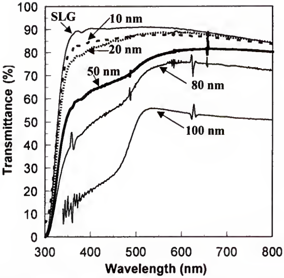

Figure 5-8. Optical transmittance spectra of CdZnS films with relative zinc composition x = 0.3 for different film thickness.

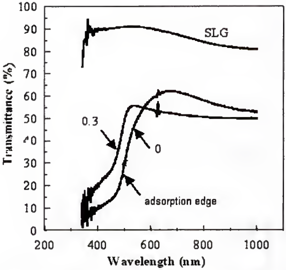

Figure 5-9. Optical transmittance spectra of CdZnS films with relative zinc compositions x = 0 (thickness d ≈ 200 nm) and x = 0.3 (d ≈ 100 nm).

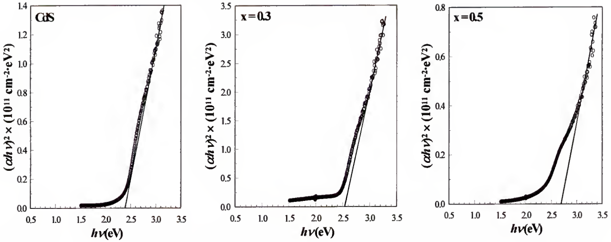

Figure 5-10. Plots of $(\alpha h\nu)^2$ versus $h\nu$ for CdZnS films with relative zinc compositions x = 0 (thickness d ≈ 200 nm), x = 0.3 (d ≈ 100 nm), and x = 0.5 (d ≈ 150 nm).

Table 5-1. Estimated energy band gaps of CdZnS films for various relative Zn composition values (x).

x	Film Thickness (nm)	E_g (eV)
0	200	2.40
0.3	100	2.55
0.5	150	2.70

Table 5-2. Measured values of electrical resistance (R), resistivity (ρ), and conductivity (σ) for as-deposited CdZnS films on ITO coated glass substrates as a function of the relative Zn compositon x.

x	Film Thickness (cm)	R (Ω)	ρ ($\Omega\cdot$cm)	σ ($\Omega\cdot$cm)$^{-1}$
0	7.0×10^{-6}	53.76	2.41×10^{3}	4.15×10^{-4}
0.1	7.0×10^{-6}	58.14	2.61×10^{3}	3.83×10^{-4}
0.3	7.0×10^{-6}	75.19	3.37×10^{3}	2.97×10^{-4}
0.5	8.0×10^{-6}	117.65	4.62×10^{3}	2.16×10^{-4}

CHAPTER 6
FABRICATION AND MEASUREMENT SYSTEMS FOR CIGS AND CGS SOLAR CELLS

6.1 Introduction

A sequential process is employed to fabricate CIGS and CGS solar cells. Samples of CIGS and CGS absorbers grown on Mo-coated SLG substrates of 2in×2in in size were provided by Energy Photovoltaic Inc. (EPV) and National Renewal Energy Laboratory (NREL) for this study. The sequential fabrication procedure is utilized to make laboratory-scale CIGS and CGS solar cells. The detailed deposition procedures of each layer are described as follows.

A computer-controlled Current-Voltage (I-V) measurement system is employed to determine the electrical output performance parameters of solar cells such as V_{oc}, J_{sc}, FF, and η. It can also be used to measure the dark current-voltage characteristics of the solar cells and determining the diode parameters such as series and shunt resistances. The computer-controlled I-V and spectral response measurement systems were used to measure photo-I-V curves and spectral response and quantum efficiency of the CIGS and CGS solar cells. A *LabVIEW* software was installed in the computer to control the measurement parameters and to perform data acquisition for the solar cells.

6.2 Fabrication of CIGS and CGS Solar Cells

Buffer layers of CdZnS with different Zn contents were deposited on the CIGS and CGS samples. The Ga content of the CIGS films was approximately 30 ~ 32%, and due to the copper-rich nature of the surface the films were covered with a thin chalcogenide

$Cu_{2-x}Se$ layer. It is well known that copper-rich CIS and CIGS films have high hole densities in the range of $10^{19} \sim 10^{20}$ cm^{-3} due to the coexistence of a semi-metallic $Cu_{2-x}Se$ impurity at the surface. A KCN etching treatment, which consists of dipping the as-deposited CIGS film in a KCN solution for several minutes, has been known to be an effective treatment to remove the Cu chalcogenide layer [90] from the surface. Prior to depositing the CdZnS buffer layer, the CIGS and CGS films were chemically treated using a 10-wt% KCN aqueous solution at room temperature for four minutes.

This is followed by deposition of a CdZnS buffer layer via CBD and then by a ZnO window layer via sputtering. A high/low resistivity i-ZnO/n-ZnO bilayer film was then deposited on these samples at EPV Inc. Next, Ni/Al grid fingers with dimensions of 50 nm/300 nm serving as front contact pads were deposited by electron-beam evaporation to obtain the finished cells. No antireflective (AR) coatings were applied.

Finally, the cells were separated with isolation of each cell by mechanical scribing. The total area for each isolated CIGS and CGS cell is 0.429 cm^2. Each cell on one single SLG substrate shares the same Mo- bottom contact, and each cell has an independent Ni/Al top contact. Figure 6-1 illustrates the CIGS or CGS solar cell structure used in fabricating solar cells with ZnO/CdZnS/CIGS (or CGS) structure. Figure 6-2 shows a completely finished CIGS cell with top contact. A cross-sectional image of the ZnO/CdZnS/CIGS/Mo/SLG solar cell obtained by the SEM is shown in Figure 6-3.

6.3 The Current-Voltage and Spectral Response Measurement Systems

6.3.1 Current-Voltage Measurement System

The solar cell under test is mounted on a sample holder. Since the surface under illumination becomes hot, the cell temperature is controlled by a chilled water loop routed through the sample holder. The temperature of the cell tested is maintained at

25±1 °C by using a thermoelectric cooler assembly with a temperature controller during the photo-I-V measurements. The sample holder contains four-terminal probes called the Kelvin connections to conduct current to and from the contacts of the cell tested. The four terminal connections allow the use of individual channels for current and voltage measurements. The probes are also connected to the current and voltage measuring devices. ELH (tungsten-halogen bulb) lamp with an integral dichroic rear reflector is used as a solar simulator to provide light intensity close to AM1.5G condition. The distance between the solar simulator and sample holder is varied to adjust the intensity of solar simulator. This gives the measured short-circuit current of the reference cell the same value as the calibrated value at the standard test condition of 100 mW/cm^2 performed at NREL.

The semi-automated I-V measurement system uses data acquisition system and software *LabVIEW* optimized for the measurements. This I-V measurement system, which is controlled by a computer with the *LabVIEW*, consists of a programmable bipolar power supply, an electrometer, and a digital multi-meter. The power supply is used as variable load, while the electrometer and multi-meter are used to measure the terminal current and voltage of the tested cells. Utilizing the *LabVIEW* software the basic device performance parameters such as V_{oc}, J_{sc}, FF, and η for the solar cells tested are obtained from the measured photo-I-V curves along with the parameters of V_m (output voltage at maximum power point), J_m (output current density at maximum power point), P_m (maximum power point).

6.3.2 Spectral Response Measurement System

The photocurrent generated by a solar cell under illumination at short circuit condition is dependent on the incident light. The quantum efficiency (QE) of the cell is used to plot the normalized photocurrent density (J_{sc}) versus the incident photon wavelength. QE is defined as the number of electron-hole pairs generated per absorbed photon and is dependent on the absorption coefficients of material and charge separation and collection in the cell. A computer-controlled QE measurement system using a grating monochrometer is employed to determine the spectral response and quantum efficiency of the solar cells in this study. The QE system scans spectral wavelengths in the range of 400 ~ 1400 nm. The monochrometer is controlled by a computer with the *LabVIEW* through the interface of GPIB and scans the spectral range described above. During the spectral response measurements, the cell area tested was covered by a monochromatic light which has a uniform intensity illumination.

To determine the spectral responsivity of the solar cell, the power or irradiance reaching the test cell at each wavelength and the photocurrent generated by the cell at each wavelength should be determined. In our system, the incident power density is measured with a calibrated silicon photodetector. The spectral response measurement is conducted under the short-circuit mode. The photocurrent generated by the test cell is converted into voltage and is measured by using a lock-in amplifier. The spectral response is calculated by using the data measured by a photodetector and the measured photocurrent of the test cell. The ratio of the photocurrent of test cell to incident beam power is the cell responsivity. This is converted to QE by using the monochrometer's wavelength (λ).

The external quantum efficiency as a function of wavelength is converted from the spectral response using the following equation,

$$QE(\lambda) = \frac{100\% \cdot h \cdot c \cdot I_{testcell}(\lambda)}{q \cdot \lambda \cdot Powerdensity_{detector} \cdot A}$$

where h is the Planck constant, c is the speed of light, q is the electronic charge, λ is the wavelength, and A is the test cell area (cm^2).

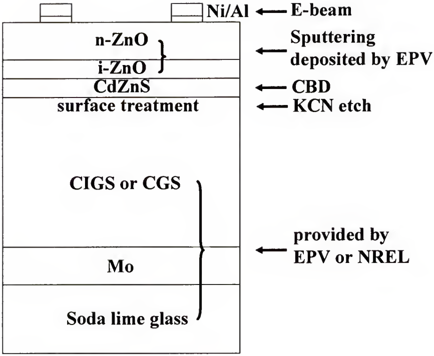

Figure 6-1. Solar cell structure used to fabricate a ZnO/CdZnS/CIGS (or CGS) cell.

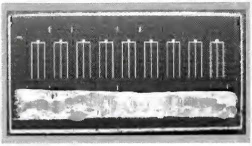

Figure 6-2. A completely finished CIGS cell with Ni/Al top contact.

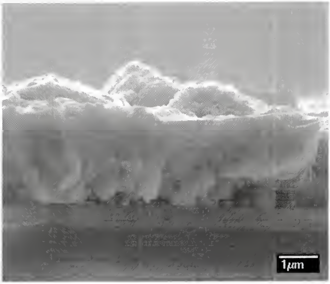

Figure 6-3. A cross-sectional SEM image of the ZnO/CdZnS/CIGS/Mo/SLG cell (10,000X).

CHAPTER 7
CURRENT-VOLTAGE AND SPECTRAL RESPONSE CHARACTERIZATIONS OF CIGS SOLAR CELLS WITH CDZNS BUFFER LAYERS

7.1 Introduction

Quaternary $Cu(In_{1-x},Ga_x)Se_2$ (CIGS) thin film material with its band gap variation from 1.04 eV ($CuInSe_2$) to 1.68 eV ($CuGaSe_2$) is one of the potential absorber candidates for use in high-efficiency thin film solar cells. Furthermore, its band gap covers the range expected for optimum conversion efficiency in photovoltaic devices. CIGS thin film solar cells with efficiencies exceeding 19% AM1.5G have been achieved [1,91]. These solar cells were typically fabricated using a CdS buffer layer deposited by CBD on the CIGS absorbers.

For fabricating a proper p-n junction solar cell, choosing an n-type buffer layer material with lattice- match to the absorber layer is very important for CIGS quaternary absorber materials. The wurtzite $Cd_{1-x}Zn_xS$ (CdZnS) ternary material gives the best lattice- match to the CIGS in the entire range of [Ga] / ([Ga] + [In]) ratio, improving device performance in the CIGS solar cells. Moreover, its band gap energy is larger than that of CdS which has been used successfully as a buffer layer in CIGS cells. The CdZnS buffer material offers a decrease in window absorption losses, and hence increases the short-circuit current in CIGS solar cells. Therefore, the replacement of CdS with CdZnS lead to the increase in quantum efficiency (QE) in the shorter wavelength region and a zero-band offset at the CdZnS and CIGS interface based on [Zn] / ([Zn] + [Cd]) ratio of CdZnS buffer layer.

The CBD technique has been used for the deposition of CdS thin films, which has produced better cell performance than other deposition methods in the CIGS solar cells.

The CdZnS buffer layer was deposited on the CIGS absorber layers by using CBD process. Zn concentration of CdZnS buffer layer was varied from x = 0 to 0.5. These CdZnS/CIGS samples were fabricated into the finished solar cells. Measurements of current-voltage (I-V) characteristics and spectral responses of the devices under AM 1.5 global spectrum for 100 mW/cm^2 irradiance at a device temperature of 25.0 ± 1°C, were carried out in this study.

This chapter presents the characteristics of I-V and QE of the CIGS solar cells with various Zn compositions in CdZnS buffer layers. The results are compared to the cells deposited with CBD CdS buffer layer.

7.2 The Effect of CIGS Absorber Surface Treatment by KCN on the Cell Performance

The cell performance parameters on CIGS absorbers treated by KCN solution are investigated and compared to those cells without KCN treatment. The KCN treatment was performed on the CIGS films before depositing the CdZnS buffer layers.

In the case where CdS is used as the buffer layer, the results given in Table 7-1 show that the CdS/CIGS cells fabricated with KCN treatment have improved the open-circuit voltage (V_{oc}), short-circuit current density (J_{sc}), and fill factor (FF), which yield better performance in terms of solar conversion efficiency (η). The CdS buffer layers were deposited using our baseline CBD process. As shown in the table, the CdS/CIGS cell of ID 21#4, which was fabricated by using the CBD process with a 30 minutes deposition time and KCN etching step, realizes the best cell performance with V_{oc} = 0.482 V, J_{sc} = 31.22 mA/cm^2, FF = 65.1 %, and η = 9.8 %.

Figure 7-1 shows the quantum efficiency for the devices of ID 39#8 and 21#4 in Table 7-1, for the purpose of comparing the effect of KCN treatment. As can be seen in this figure, the quantum efficiency of the device utilizing the KCN treatment is higher than that of the device without the KCN treatment.

In the case in which the CdZnS is used as buffer layer, Table 7-2 shows that CdZnS/CIGS cells fabricated with KCN treatment also have improved performance parameters.

7.3 Current-Voltage and Quantum Efficiency of CIGS Cells with CdZnS Buffer Layers

7.3.1 The Effect of Buffer Layer Thickness on the Cell Performance

The effect of CdZnS buffer layer thickness on the performance of CdZnS/CIGS cells can be assessed from Figure 7-2, which shows the photo-J-V characteristics of cells with relative zinc composition $x = 0.3$ and CBD deposition times of 40, 50, and 60 minutes. The buffer layer deposition times were increased from 40 to 60 minutes. The fill factor was found to increase when the deposition time reached 60 minutes.

Table 7-3 shows the performance parameters of these cells. The tested CdZnS/CIGS cells achieved higher short-circuit currents as compared to those of the CdS/CIGS cells reported in Table 7-1, while at the same time realizing comparable or slightly higher open-circuit voltages.

7.3.2 The Effect of Different Zn Compositions of CdZnS Buffer Layer on the Cell Performance

Increasing the relative zinc content x can increase the energy band gap of CdZnS, and results in band gap values higher than that of CdS. In fact, as discussed in Chapter 5, CdZnS film with $x = 0.5$ has an energy band gap of 2.7 eV, a value that is higher than that of CdS ($E_g = 2.4$ eV). Consequently the CdZnS/CIGS cells are expected to have a higher short-circuit current than CdS/CIGS cells because of the higher quantum efficiency and photocurrent in the shorter wavelength region.

Table 7-4 shows the dependence of the cell performance parameters on the relative zinc composition values of x = 0, 0.1, 0.2, 0.3, 0.4, and 0.5. The CIGS layers were etched by KCN before the CBD buffer layer growth. The best cell in each CIGS sample fabricated was obtained from the photo-I-V measurement and used to compare the performance parameters as shown in Table 7-4. Other cells in each CIGS sample produced a similar range of performance parameters as the best cell. All CIGS absorber films provided were grown in the same condition with Ga content of around 30 ~ 32%. Therefore, it is expected that the CIGS absorber films used in this study have similar film quality.

Relevant subsets of the data in Table 7-4 are plotted in Figure 7-3 as an alternative visualization of the results. Note from Table 7-4 and Figure 7-3 that the CdZnS/CIGS cell with a relative zinc composition of x = 0.2 has achieved a conversion efficiency of approximately 13% under AM1.5G condition. Also note that starting with the composition x = 0 (corresponding to a CdS/CIGS cell) the efficiency increases with increasing relative zinc content in the CdZnS/CIGS cell up to the composition x = 0.2. The data shows a decrease in conversion efficiency for compositions x = 0.3 and x = 0.4, and finally a drastic decrease in efficiency for the zinc-rich CdZnS/CIGS cell with x = 0.5.

The CdZnS buffer layer with a 20% Zn content, which provides a higher energy band gap than CdS, contributes to improve in the values of J_{sc} and V_{oc}, resulting in a higher efficiency than the CIGS cells with a CdS and other Zn content buffer layers as shown in Table 7-4. In addition to the results described above, a smaller thickness of the buffer film with composition of x = 0.2 (*see* Table 7-4), it is possible to explain the fact that a relatively sharp change in efficiency was observed between the composition and efficiency of the cells with x = 0.3 and x = 0.4. It is clear, nevertheless, that a zinc content of x = 0.5 is no longer beneficial for the purpose of efficiency enhancement. Therefore, the efficiency plot given in Figure 7-3 supports the claim that CdZnS/CIGS cells benefit from the increase of Zn content up to a value of x = 0.3. A reduction in efficiency was found at a Zn content of x = 0.5 or higher. Figure 7-4 shows the photo-J-V characteristics of CdZnS/CIGS cells listed in Table 7-4.

As mentioned above, the reason for using CdZnS buffer layers (which has a wider band-gap energy than CdS) is the potential for increasing the photo-current generation particularly in the spectral region for wavelengths less than 550 nm. A comparison of the quantum efficiency of selected cells is shown in Figure 7-5, where spectral response curves are given for four CdZnS/CIGS cells with Zn contents x = 0, 0.2, and 0.5. At shorter wavelengths, all the CIGS cells deposited with CdZnS buffer layers have better quantum efficiency than the cells fabricated with the CdS buffer. Furthermore, in the shorter wavelengths the quantum efficiency of CdZnS/CIGS cells becomes higher as the relative zinc content x increases, as can be expected from the widening of the band gap energy of CdZnS caused by the additional presence of zinc. The small difference in cut-off wavelength can be attributed to the difference in Ga content in the CIGS absorber layers.

Further studies and optimization of the CdZnS buffer layer thickness and deposition conditions to improve the film quality are needed for better understanding of this buffer layer and achieving the highest performance possible.

7.4 Summary and Conclusions

To study the effect of $Cd_{1-x}Zn_xS$ buffer layers on the performance of CIGS cells, a series of buffer films with relative Zn content of x = 0 (CdS), 0.1, 0.2, 0.3, 0.4, and 0.5 were deposited on the CIGS samples provided by EPV Inc., and a detailed study of the current-density/voltage characteristics and spectral response (QE) was carried out.

It was observed that CIGS films treated with KCN etching preceding the buffer CBD step lead to improved cell performance for CIGS cells deposited with either CdS or CdZnS buffers. Adding Zn in the CdZnS buffer layer material results in improvement of the performance of CdZnS/CIGS cells as compared to a Zn-free CdS/CIGS cell.

In particular, a CdZnS/CIGS cell with relative zinc composition x = 0.2 achieved a conversion efficiency of approximately 13 % under AM1.5G conditions, showing improved V_{oc}, J_{sc}, and FF values compared to the CdS/CIGS cell and CdZnS/CIGS cells with different Zn contents. The 13 % efficiency realized by using x = 0.2 in the CdZnS/CIGS cell represents a 30% increase in efficiency over the reference CdS/CIGS solar cell used in this study. Furthermore, the quantum efficiency of CdZnS/CIGS cells becomes higher at shorter wavelengths compared to the CdS/CIGS cell as the relative zinc content x increases, until a maximum relative zinc composition equal to x = 0.5.

Table 7-1. Performance of CdS/CIGS cells with and without a KCN treatment of the CIGS absorber layers.

Device ID	Device Area (cm^2)	Irradiance (mW/cm^2)	KCN Etch	x	Deposition Time (min)	V_{oc} (V)	J_{sc} (mA/cm^2)	FF (%)	η (%)
39#8	0.429	100	No	0	30	0.420	28.04	51.47	6.06
21#4	0.429	100	Yes	0	30	0.482	31.22	65.10	9.80
22#1	0.429	100	Yes	0	40	0.487	32.82	59.45	9.51

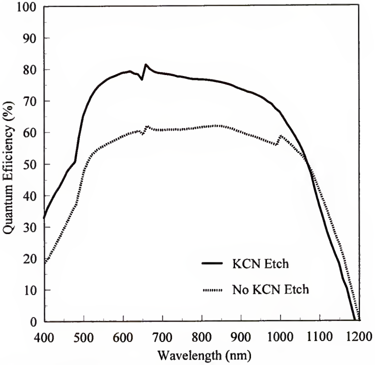

Figure 7-1. Quantum efficiency for the CdS/CIGS solar cells shown in Table 7-1 (Device ID: 39#8 and 21#4).

Table 7-2. Performance of CdZnS/CIGS cells with and without a KCN treatment of the CIGS absorber layers.

Device ID	Device Area (cm^2)	Irradiance (mW/cm^2)	KCN Etch	x	Deposition Time (min)	V_{oc} (V)	J_{sc} (mA/cm^2)	FF (%)	η (%)
13#B2	0.100	101.5	No	0.3	45	0.502	30.19	50.68	7.56
14#A2	0.090	102.1	Yes	0.3	45	0.518	31.24	63.40	10.05

Note: For the cells in Table 7-2, I-V measurements were performed at EPV.

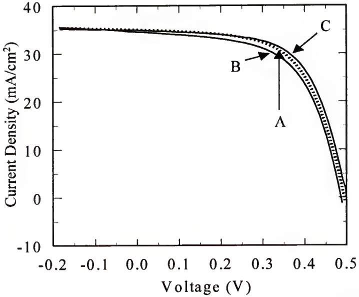

Figure 7-2. Photo-J-V characteristics of CdZnS/CIGS cells using different deposition times and relative zinc composition x = 0.3. The CBD-grown CdZnS buffer layers were fabricated with deposition times of 40 min (A), 50 min (B), and 60 min (C), in an 85 °C bath.

Table 7-3. Performance parameters of CdZnS/CIGS cells as a function of different deposition times for a relative zinc composition x = 0.3 in the buffer layer.

Device ID	Device Area (cm^2)	Irradiance (mW/cm^2)	KCN Etch	x	Deposition Time (min)	V_{oc} (V)	J_{sc} (mA/cm^2)	FF (%)	η (%)
(A)33#3	0.429	100	Yes	0.3	40	0.493	35.16	60.98	10.57
(B)30#1	0.429	100	Yes	0.3	50	0.487	34.56	60.06	10.11
(C)32#1	0.429	100	Yes	0.3	60	0.501	34.89	66.81	11.67

Table 7-4. Performance parameters of CdZnS/CIGS cells as a function of the relative zinc content x of the buffer layer.

Device ID	Device Area (cm^2)	Irradiance (mW/cm^2)	KCN Etch	x	Thickness (nm)	V_{oc} (V)	J_{sc} (mA/cm^2)	FF (%)	η (%)
(A)21#4	0.429	100	Yes	0	40 ~ 50	0.482	31.22	65.10	9.80
(B)38#8	0.429	100	Yes	0.1	60 ~ 70	0.517	32.85	66.31	11.25
(C)33A#8	0.429	100	Yes	0.2	~ 40	0.526	35.60	69.53	13.02
(D)32#1	0.429	100	Yes	0.3	60 ~ 70	0.501	34.89	66.81	11.67
(E)33B#3	0.429	100	Yes	0.4	60 ~ 70	0.515	34.74	66.85	11.97
(F)31#1	0.429	100	Yes	0.5	60 ~ 70	0.494	35.17	59.68	10.36

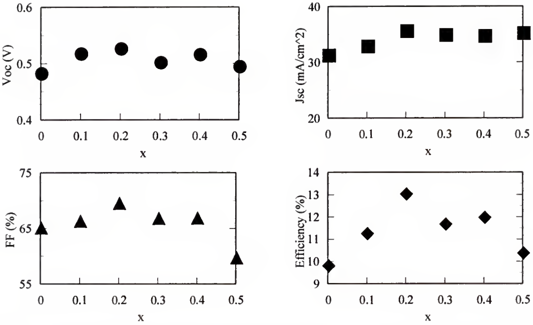

Figure 7-3. Performance parameters of CdZnS/CIGS cells as a function of the relative zinc content x (graphical representation of the data given in Table 7-4).

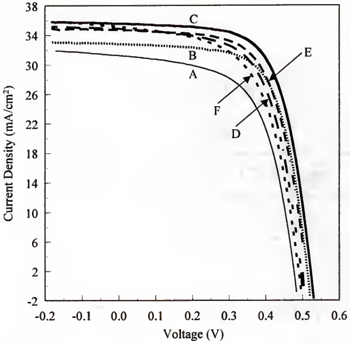

Figure 7-4. Photo-J-V characteristics of CdZnS/CIGS cells with different relative zinc contents x = 0 (A), x = 0.1 (B), x = 0.2 (C), x = 0.3 (D), x = 0.4 (E), and x = 0.5 (F).

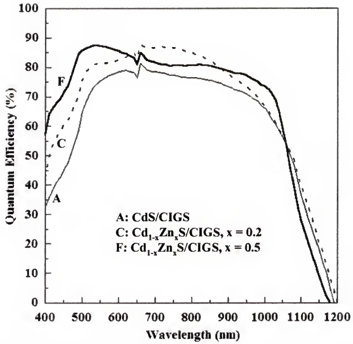

Figure 7-5. Quantum efficiency comparison between a CdS/CIGS solar cell (A), and CdZnS/CIGS solar cells with relative zinc composition x = 0.2 (C) and x = 0.5 (F).

CHAPTER 8
CURRENT-VOLTAGE AND SPECTRAL RESPONSE CHARACTERIZATIONS OF CGS SOLAR CELLS WITH CDZNS BUFFER LAYERS

8.1 Introduction

Cu-chalcopyrite semiconductors with general composition of $Cu(In_{1-x},Ga_x)(Se_y,S_{1-y})_2$ provide a wide range of band gaps ranging from 1.04 eV for $CuInSe_2$ to 2.4 eV for $CuGaS_2$. A direct band-gap material with E_g = 1.68 eV and a very high optical absorption coefficient ($\alpha > 10^4$ cm^{-1} for $\lambda < 700$ nm [18]), $CuGaSe_2$ (CGS) has received considerable attention as a promising candidate for use as an absorber material of top cell in tandem solar cells. Schottky diodes [92] and heterojunctions based on CGS single crystals [93,94] or polycrystalline thin films [95,96] have been fabricated with conversion efficiencies up to 6.7% [94]. Although there were some early works on CGS cells, it was not until 1996 that a reasonable cell efficiency was reported. Single crystal CGS cell such as ZnO/CdS/CGS produced an efficiency of 9.7%, an open-circuit voltage of 0.946 V, a short-circuit current density of 15.5 mA/cm^2, and a fill factor of 66.5% under AM1.5G condition [66]. Polycrystalline CGS cell with an efficiency of 9.32% and an open-circuit voltage of 0.87 V were reported in 1997 [97]. New world record total-area efficiency for a surface-modified CGS solar cell was achieved with the performance parameters of V_{oc} = 0.823 V, J_{sc} = 18.61 mA/cm^2, FF = 66.77%, and total-area-efficiency of η = 10.2% AM1.5G [1].

The device performance for the wide band-gap CGS cells is inferior to the best CIGS cells [1], in spite of efforts described above. Based on reported experimental works, the most obvious limiting performance characteristic of CGS cells is the low open-circuit voltage (V_{oc}). An empirical expression for the V_{oc} of CGS and CIGS cells can be approximately described by $V_{oc} \approx (E_g/q)-0.5$ V [19]. A V_{oc} of ~ 1.2 V is predicted for the CGS cells using this equation. However, the reported values of V_{oc} for CGS cells are smaller than the predicted values [2]. For smaller band gap CIGS absorbers with E_g $\leq$1.3 eV and Ga content of $\approx$ 25-30%, the value of V_{oc} increases at the same rate as the band gap energy of CIGS absorbers. For wider band-gap CIGS absorbers (*i.e.*, $E_g \geq 1.3$ eV), the value of V_{oc} does not increase at the same rate as E_g, and hence device efficiency is reduced. Current collection depending on voltage results in poor fill factor, and gives lower cell efficiency for CGS absorbers with high Ga content such as CGS cells [98].

As-deposited p-type CIS films show an n-type In-rich inversion layer at the surface [41], while CGS films do not show the same surface inversion. CdS has been used widely as a buffer layer for both CIGS (Ga < 30%) and CGS solar cells. For CIGS-based cells with CdS buffer layers, increasing the Ga content changes the conduction band offset at the heterojunction interface from a small spike for the CIS cells to a cliff for the CGS cells. Ideally, the difference in electron affinities, $\Delta\chi = \chi_n - \chi_p$, should be equal to zero. A negative $\Delta\chi$ ($\chi_n < \chi_p$) produces a conduction band "spike". If $\Delta\chi$ is positive ($\chi_n > \chi_p$) as in CGS cells, the V_{oc} is reduced and the performance of the CGS cell is degraded. The absence of an inverted surface layer in CGS cells and the change of a barrier for the injection of electrons at the heterojunction increase junction related recombination rates, which leads to the decrease of cell efficiency. Furthermore, the lattice match between the CdS buffer and the CGS absorber is poor. The improved performance of CdS/CGS cells upon increasing the CdS CBD temperature was clearly correlated to the improvement in the quality of this interface at an increased deposition temperature [21]. Therefore, studies of alternative buffer layers to replace the CdS for the wide band gap CGS solar cells should be a priority.

The addition of Zn to the most widely used CdS buffer layer material is logical. First, the addition to Zn decreases the lattice constant with a match to CGS occurring at near the equimolar composition, the exact matched composition depending on whether the $Cd_{1-x}Zn_xS$ is cubic or hexagonal. Second, the addition of Zn increases the band gap and produces a more favorable conduction band alignment. It has been demonstrated that adding Zn to CdS enhances both the open-circuit voltage and photocurrent of the cells to give higher conversion efficiency [86].

Based on studies of the CdZnS film characterizations depicted in Chapter 5 and the characteristics of I-V and QE of CIGS cells in Chapter 7, it is suggested that a Zn content of $x = 0.2$ to 0.3 is the optimal Zn- content for the cell performance. The buffer films with a maximum relative zinc composition equal to $x = 0.5$ developed poor color, bad adhesion, and other undesirable features. Therefore, the CdZnS buffer layer with a Zn content of $x = 0.3$ was used for fabricating CGS cells in this Chapter. CdZnS buffer layer material was grown by CBD on CGS absorbers and subsequently processed into cells for the photo-J-V and QE measurements.

This chapter presents the surface characterization of CGS films and the characteristics of I-V and QE of the CGS solar cells with Zn composition $x = 0.3$ for the CdZnS buffer layers. The results are compared to the cells deposited with CBD CdS buffer layers.

8.2 Surface Morphology of a CGS Film and a CdZnS Film on CGS

CGS absorber samples provided by the NREL were used to fabricate CdZnS/CGS and CdS/CGS solar cells. Some of the CGS absorber films were etched with KCN solution to assess the effect of such a surface-preparation step. For the purpose of quantifying the effect of KCN etching, the surface morphologies of CGS/Mo/glass and CdZnS/CGS/Mo/glass structures treated with a 10% KCN solution for four minutes were characterized using SEM and AFM techniques.

Figures 8-1 shows the SEM micrograph of the CGS film surface in the CGS/Mo/glass structure, and Figure 8-2 shows the surface of the $Cd_{1-x}Zn_xS$ film with zinc content $x = 0.1$ in the CdZnS/CGS/Mo/glass structure. The thickness of CdZnS film is estimated to lie in the range of 60 to 70 nm. The SEM study reveals that a rough surface is observed on the CGS film (*cf.* Figure 8-1), whereas the surface of the CdZnS film is smoother (*cf.* Figure 8-2).

Images obtained via AFM of the two etched films are shown in Figures 8-3 and 8-4, respectively. The scanned three-dimensional images (10 ×10 μm) of Figure 8-3 show the sharp roughness of the KCN etched CGS film surface. In contrast, the relatively smoother surface of the $Cd_{1-x}Zn_xS$ film ($x = 0.1$) deposited on the KCN-etched CGS is shown in Figure 8-4.

8.3 Current-Voltage Characteristics and Quantum Efficiency of CGS Cells with CdZnS Buffer Layers

Functional CGS solar cells were fabricated in an ensuing study by depositing either a CdS buffer layer or a $Cd_{1-x}Zn_xS$ buffer layer with a relative Zn content of $x = 0.3$ on CGS absorbers. Some of the absorbers were subjected to a 4 minutes etching step using a solution of 10 % KCN. Bilayer films of ZnO were then deposited on these samples by sputtering technique at EPV Inc. Front contacts in the form of Ni/Al grid fingers with dimensions of 50 nm/300 nm were deposited by electron-beam evaporation.

The photo-J-V measurements were carried out on these cells under AM1.5G (100 mW/cm^2) irradiance at a device temperature of 25.0 ± 1 °C. The results are summarized in Table 8-1. The results show that KCN-treated CdS/CGS and CdZnS/CGS cells have improved V_{oc}, J_{sc}, and FF values, and a higher conversion efficiency. Note that the J_{sc} has also improved for the CdZnS/CGS cell with absorber subjected to a KCN etch, whereas, in contrast, the J_{sc} of the CdS/CGS cell does not show significant improvement when the KCN etch step is applied.

Figure 8-5 illustrates the photo-J-V characteristics of the CdS/CGS and CdZnS/CGS cells fabricated using the KCN etch step corresponding to the devices with ID S2381-A2-K21 and S2381-B1-K31 shown in Table 8-1. Figure 8-5 shows that the V_{oc} value of the CdZnS/CGS cell with $x = 0.3$ increases by 80 mV relative to that of the CdS/CGS cell, while the J_{sc} value increases by 0.43 mA/cm^2. In fact, the CdZnS provides a better conduction-band offset on CGS cells than that of CdS buffer layer [43]. As shown in Figure 8-5, it is clearly demonstrated that CdZnS buffer layer improves V_{oc} which is attributed to the reduced conduction band discontinuity at the junction.

The replacement of CdS by CdZnS decreases the window layer absorption losses, and hence increases the values of J_{sc} and V_{oc} in the CGS cell. Figure 8-6 shows the quantum efficiency of the CdS/CGS and CdZnS/CGS cells shown in Figure 8-5 (*i.e.*, for devices with ID S2381-A2-K21 and S2381-B1-K31 in Table 8-1). It is clearly shown in this figure that the CdZnS/CGS cell has effectively increased the current generation at shorter wavelengths (*i.e.*, $\lambda < 500$ nm), resulting in a higher J_{sc} value due to the higher quantum efficiency. It is also observed that the quantum efficiency at $\lambda > 500$ nm is limited to a maximum around 70%, which is presumably caused by the consequence of losses in the collection of the photo-generated carriers near the surface region. This could be due to high recombination velocity and low diffusion length in the near surface region.

Further studies and optimization of CdZnS buffer layer thickness and deposition conditions are needed for improving the performance of this buffer material and for achieving the highest-possible performance of CdZnS/CGS solar cells.

Another set of CGS cells was fabricated also using CGS films provided by NREL. A CdS and a CdZnS ($x = 0.3$) buffer layer were deposited after KCN etching on two CGS films. Table 8-2 shows the results that CdZnS/CGS cell has improved V_{oc} and FF values as compared to the CdS/CGS cell, but shows no improvement in J_{sc} value. The most noticeable result is an increase in efficiency by 3 %. Table 8-2 shows that the V_{oc} value of the CdZnS/CGS cell with $x = 0.3$ increases by 175 mV relative to that of the CdS/CGS cell. The increase in V_{oc} with increasing Zn content is linked to the reduced conduction band discontinuity at the junction between the CdZnS and CGS and the improvement in the built-in voltage. Further, it is expected that the changes of electrical resistivity and crystalline structure and additionally an increased series resistance of this CdZnS film during CBD growth process might be responsible for the decrease in J_{sc} value for the CdZnS/CGS cells listed in Table 8-2.

It should be pointed out that a comparison of the two devices listed in Table 8-2 (Device ID: S2259 and S2283) might not be fair since those CGS films provided are from different substrates, which produce different cell performance when they are fabricated into devices, because of different CGS absorber quality. A comparison of the performance of CdS/CGS and CdZnS/CGS cells with KCN treatment is summarized in

Table 8-1. The CdS/CGS and CdZnS/CGS cells listed in Table 8-2 have higher J_{sc} values than those given in Table 8-1, while at the same time showing lower V_{oc} values.

8.4 Summary and Conclusions

The effect of CdZnS buffer layers on CGS cells was characterized for the case where the relative Zn content was fixed at $x = 0.3$. A CdZnS layer was deposited over a CGS absorber provided by NREL. It is shown that KCN treatment before the CBD growth of CdZnS buffer layer is a desirable processing step for both CdS/CGS and CdZnS/CGS cells, bringing improved conversion efficiencies due to better V_{oc}, J_{sc}, and FF properties. In particular, a CdZnS/CGS cell with relative zinc composition $x = 0.3$ achieved a conversion efficiency of approximately 5.3% under AM1.5G conditions, realizing better V_{oc}, J_{sc}, and FF values relative to the reference Zn-free CdS/CGS cell. The 5.3% efficiency realized by the $x = 0.3$ CdZnS/CGS cell represents an increase in efficiency by a factor of 1.25 over the reference Zn-free CdS/CGS solar cell. It is also shown that the CdZnS/CGS cell has increased the photo-current generation in the shorter wavelengths (*i.e.*, $\lambda < 500$ nm) relative to the CdS/CGS cell. In both the CIGS and CGS cases, the experimental results showed that from a viewpoint of device performance it was beneficial to pre-treat the absorber layer with a 10% KCN solution before CBD growth of buffer layers. Both the CIGS and CGS absorber films used in this study were provided by EPV Inc., and NREL, respectively.

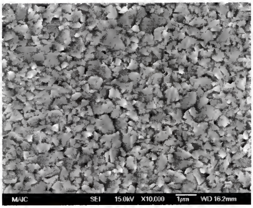

Figure 8-1. SEM micrograph of the surface of a CGS film etched with a 10% KCN solution (10,000X).

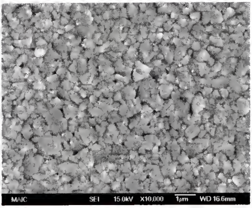

Figure 8-2. SEM micrograph of the surface of a $Cd_{1-x}Zn_xS$ film ($x = 0.1$) deposited on a CGS absorber etched with a 10% KCN solution (10,000X).

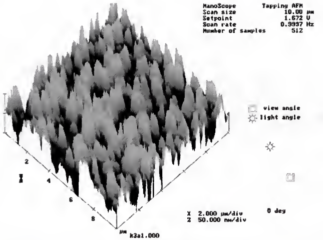

Figure 8-3. AFM image of the surface of a CGS film etched with a 10% KCN solution.

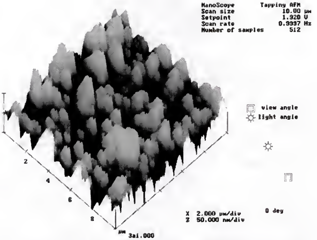

Figure 8-4. AFM image of the surface of a $Cd_{1-x}Zn_xS$ film ($x = 0.1$) deposited on a CGS absorber etched with a 10% KCN solution.

Table 8-1. Performance of CdS/CGS and CdZnS/CGS cells with and without KCN treatments on the CGS absorber layers (AM1.5G, 100 mW/cm^2).

Device ID	Device Area (cm^2)	KCN Etch	x	Deposition Time (min)	V_{oc} (V)	J_{sc} (mA/cm^2)	FF (%)	η (%)
S2381-A2-22	0.429	No	0 (CdS)	20	0.352	15.05	41.87	2.22
S2381-A2-K21	0.429	Yes	0 (CdS)	20	0.533	14.91	53.47	4.25
S2381-B1-32	0.408	No	0.3	45 ~ 50	0.394	12.22	35.96	1.73
S2381-B1-K31	0.408	Yes	0.3	45 ~ 50	0.613	15.34	56.70	5.33

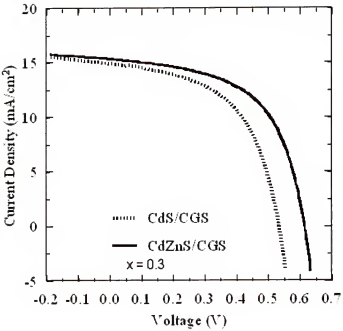

Figure 8-5. Photo-J-V characteristics of a CdS/CGS cell and a CdZnS/CGS cell with relative zinc composition x = 0.3.

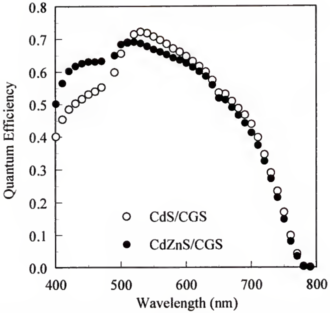

Figure 8-6. Quantum efficiency vs. wavelength for the cells shown in Figure 8-5.

Table 8-2. The performance of CdS/CGS and CdZnS/CGS cells with KCN treatments on the CGS absorber layers (AM1.5G, 100 mW/cm^2).

Device ID	Device Area (cm^2)	KCN Etch	x	Deposition Time (min)	V_{oc} (V)	J_{sc} (mA/cm^2)	FF (%)	η (%)
S2259	0.429	Yes	0 (CdS)	20	0.296	17.22	30.71	1.60
S2283	0.429	Yes	0.3	50 ~ 55	0.471	16.06	38.38	3.00

CHAPTER 9
SUMMARY AND FUTURE STUDIES

9.1 Summary and Conclusions

Device modeling and simulation studies for a mechanically-stacked CGS/CIGS tandem cell have been carried out in this work using the AMPS-1D simulation program. A CIGS cell with a double band-gap graded CIGS absorber and a CGS cell with a uniform CGS absorber have been used as the bottom and top cells of a tandem cell structure, respectively. It is shown that values of J_{sc} and η for the CIGS bottom cell with a CGS top cell were found to decrease by more than 50 % compared to that of the stand-alone CIGS cell. The simulation results of CGS/CIGS tandem cell performance suggest that a 25% AM1.5G conversion efficiency could be achieved by using a CGS top cell with η > 16% and an optimized CIGS bottom cell with efficiency of 8 to 10 %. Additionally, a comparison of the simulation results with the reported experimental data shows a good agreement in the photo-J-V and QE curves between the modeling and the experimental data for the single-junction CIGS and CGS cells.

Structural, surface morphological, optical, and electrical analyses show that CdZnS films with relative zinc composition of approximately x = 0.3 appear to have significant benefits when CdZnS films were used as buffer layers for the CIGS and CGS solar cells. It is concluded that CdZnS films with relative zinc composition x = 0.3 showed better than 80% transmittance for wavelengths longer than 600 nm with film thicknesses less than 50 nm. Because of their high transmittance, CdZnS can be useful as a buffer layer for the CGS and CIGS cells. Therefore, it can be concluded from the structural, surface, optical, and electrical analyses that $Cd_{1-x}Zn_xS$ film with relative Zn content x = 0.3 is an excellent candidate as buffer-layer material for the CIGS and CGS solar cells.

The CIGS solar cells have been fabricated using $Cd_{1-x}Zn_xS$ buffer layers with Zn content values x = 0 (CdS), 0.1, 0.2, 0.3, 0.4, and 0.5, and a comprehensive device characterization has carried out using the current density-voltage and quantum efficiency measurements. In particular, the CdZnS/CIGS cell with a relative zinc composition x = 0.2 has achieved a conversion efficiency of approximately 13 % under AM1.5G conditions, showing improved values of V_{oc}, J_{sc}, and FF as compared to the reference CdS/CIGS cell and other CdZnS/CIGS cells with different Zn contents. Moreover, the quantum efficiency of the CdZnS/CIGS cells becomes higher at short wavelengths compared to the CdS/CIGS cell as the relative zinc content x increases up to a maximum relative zinc composition equal to x = 0.5.

CdZnS/CGS solar cells have been fabricated using CdZnS buffer layers with Zn contents of x = 0 and 0.3. The resulting device with Zn-content given by x = 0.3 has achieved a conversion efficiency that is 25% higher than the efficiency of a CdS/CGS cell. It is also shown that the CdZnS/CGS cell has produced higher photocurrent in the shorter wavelengths (*i.e.*, $\lambda < 500$ nm) relative to the CdS/CGS cell. Furthermore, values of V_{oc} of the CdZnS/CGS cell have increased as compared to the CGS cell deposited with CBD CdS buffer layer.

9.2 Future Studies

The goal of this research is to identify the critical paths for developing a low cost and high efficiency two-junction tandem solar cell based on CGS and CIGS material systems. Modeling and simulation of a mechanically-stacked four-terminal two-junction CGS/CIGS tandem cell have been carried out in this work. Future studies can extend to investigate a two-terminal two-junction monolithically-cascaded CGS/CIGS tandem solar cell. As a result of our studies, as well as others, it is clear that the most critical issue is to develop a high-performance CGS top cell and a high-quality tunnel junction for a monolithic CGS/CIGS tandem cell. To improve V_{oc} and J_{sc} of the CGS top cell, as mentioned in Chapters 2, 7, and 8, the studies of alternative buffer layers instead of CdS buffer layer are necessary. In this work the CdZnS buffer layers have been investigated for use in a wide band-gap CGS top cell, and enhanced performance of CIGS and CGS cells has been observed using CdZnS buffer layers. ZnSe and Zn(Se,OH) buffer layers are also promising candidates for this purpose since they have good lattice match to the CGS absorber layer and produce favorable conduction band spikes. Therefore, the ZnSe and Zn(Se,OH) buffer layers deposited by CBD process are suggested as practical replacement for the CdS buffer layer in the fabrication of CGS solar cells. These buffer layers can also be employed for the CIGS solar cells to further improve blue region response.

The tunnel junction requires a material with low resistance, transparent, defect free, heavy doping, and good lattice match to the top and bottom cell absorber materials (a_o = 5.61 Å for CGS, a_o = 5.78 Å for CIS), and has a band gap energy equal or greater than the top cell absorber. The stability of the tunnel junction during layer deposition processes is a crucial issue for achieving the maximum conversion efficiency of the monolithic tandem solar cells.

It is suggested that a thin tunnel junction with thickness of 10 ~ 30 nm for each p^+ and n^+ layer is desired to minimize optical absorption in the tunnel junction. However, the thin tunnel junction may not have sufficient electron and hole densities to provide a large tunneling current density. For two-terminal tandem cell configurations, current matching may be obtained either by thinning down the top cell to limit photon absorption in the top cell or by allowing some of the incident radiation to reach to the bottom cell.

It was observed that when the concentration of cadmium ion (Cd^{2+}) increases in the solution during the CBD-CdS process, the rate of deposition increases, offering better optical, structural, and adhesive properties [99]. It was also shown that annealed CdS films with the increase of Cd^{2+} concentration exhibit increase in carrier density up to 5×10^{19} cm^{-3} with decreased carrier mobility [99]. This simple approach utilized by intrinsic defects through stoichiometry control during the CBD process can be explored to deposit a high doping density in the n^+ CdZnS layer in the tunnel junction.

Another approach to obtain a higher doping, n^+ layer through the CBD process is to dope the films using extrinsic dopants. Many shallow donors such as the elements of Cl, Br, and I can easily be incorporated into the bath during the CBD process by the choice of salt, (e.g., $CdCl_2$). It can be explored how to incorporate the dopants into the CBD process. Other promising candidates for the dopants are metallic In and Ga, which are compatible with the top CGS layer and produce donor levels in CdS. Therefore, the influence of the solution II/VI ratio and the addition of In or Ga on the carrier density can be investigated.

There are several reports in the literature of high doping n^+ CdZnS films grown by a conventional low pressure MOVPE (Metal-Organic Vapor Phase Epitaxy). Iodine doping to the CdZnS films was reported by using ethyl iodide (C_2H_5I) as a donor dopant, obtaining a carrier density of ~ 10^{19} cm^{-3} for the doped CdZnS films [76,100]. Another doping experiment using triethyl indium (TEIn) was reported with the obtained carrier density of 4×10^{18} cm^{-3} [101]. These reports give a very good approach to grow and achieve a high doping density in n^+ CdZnS layer in the tunnel junction.

A simple structure for the p^+ CGS/ n^+ CdZnS tunnel junction between the CGS top cell and the CIGS bottom cell can be modeled and simulated numerically. Since the structure of the tunnel diode is not complicated one can use the AMPS-1D program to study the current-voltage (I-V) characteristics and the peak current density of the p^+ CGS/ n^+ CdZnS tunnel diode. For the modeling and simulation of the monolithic cascaded CGS/CIGS tandem cell with a p^+ CGS/ n^+ CdZnS tunnel junction, one can use Medici 2-D device simulation program. The spectral responses of a CIGS bottom cell covered with a p^+ CGS/ n^+ CdZnS tunnel junction and a CGS top cell can be also investigated.

LIST OF REFERENCES

[1] J. AbuShama, R. Noufi, S. Johnston, S. Ward, and X. Wu, Conference Record of the Thirty-First IEEE Photovoltaic Specialist Conference, Lake Buena Vista, FL, pp. 299-302, 2005.

[2] S. Siebentritt, Thin Solid Films, Vol. 403-404, pp. 1-8, 2002.

[3] M. Ristova, Y. Kuo, H.H. Lee, and J.Y. Tewg, Semiconductor Science and Technology, Vol. 20, No. 10, pp. 1005-1009, 2005.

[4] Sheng S. Li, Semiconductor Physical Electronics, Plenum, New York, 1993.

[5] M.E. Nell and A.M Barnett, IEEE Transactions on Electron Devices, Vol. ED-34, No. 2, pp. 257-266, 1987.

[6] S.R. Kurtz, P. Faine, and J.M. Olson, Journal of Applied Physics, Vol. 68, No. 4, pp. 1890-1895, 1990.

[7] J.C.C. Fan, B-Y. Tsaur, and B.J. Palm, Conference Record of the 16th IEEE Photovoltaic Specialists Conference, San Diego, CA, pp. 692-701, 1982.

[8] T.J. Coutts, K.A. Emery, and J.S. Ward, Progress in Photovoltaics: Research and Applications, Vol. 10, No. 3, pp. 195-203, 2002.

[9] P.V. Meyers, C.H. Liu, L. Russell, V. Ramanathan, R.W. Birkmire, B.E. McCandless, and J.E. Phillips, Conference Record of the 20th IEEE Photovoltaic Specialists Conference, Las Vegas, NV, pp. 1448-1451, 1988.

[10] R.P. Gale, R.W. McClelland, B.D. Dingle, J.V. Gormley, R.M. Burgess, N.P. Kim, R.A. Mickelsen, and B.J. Stanbery, Conference Record of the 21th IEEE Photovoltaic Specialists Conference, Kissimmee, FL, pp. 53-57, 1990.

[11] R.W. Birkmire, L.C. Dinetta, J. Meakin, J.E. Phillips, Conference Record of the 17th IEEE Photovoltaic Specialists Conference, Kissimmee, FL, pp. 1406-1407, 1984.

[12] B.E. McCandless, R.W. Birkmire, W.A. Buchanan, J.E. Phillips, and R.E. Rocheleau, Conference Record of the 20th IEEE Photovoltaic Specialists Conference, Las Vegas, NV, pp. 381-384, 1988.

[13] J.L Gray, Conference Record of the 21st IEEE Photovoltaic Specialists Conference, Kissimmee, FL, pp. 345-347, 1990.

[14] R.J. Schwartz and J.L. Gray, Conference Record of the 26th IEEE Photovoltaic Specialists Conference, Anaheim, CA, pp. 871-874, 1997.

[15] J. Hou, S.J. Fonash, M. Ghosh, J. Xi, T. Liu, and F. Kampas, Conference Record of the 1st World Conference on Photovoltaic Solar Energy Conversion, Waikoloa, HI, pp. 445-448, 1994.

[16] S. Bae and S.J. Fonash, Conference Record of the 1st World Conference on Photovoltaic Solar Energy Conversion, Waikoloa, HI, pp. 484-487, 1994.

[17] W.H. Bloss, J. Kimmerle, F. Pfisterer, and H.W. Schock, Conference Record of the 17th IEEE Photovoltaic Specialists Conference, Kissimmee, FL, pp. 715-720, 1984.

[18] J.L. Shay and J.H. Wernick, Ternary Chalcopyrite Semiconductors: Growth, Electronic Properties, and Applications, Pergamon Press, Oxford, 1975.

[19] V. Nadenau, U. Rau, A. Jasenek, and H.W. Schock, Journal of Applied Physics, Vol. 87, No. 1, pp. 584-593, 2000.

[20] M.E. Beck, T. Weiss, D. Fischer, S. Fiechter, A. Jäger-Waldau, and M.Ch. Lux-Steiner, Thin Solid Films, Vol. 361-362, pp. 130-134, 2000.

[21] A. Jasenek, U. Rau, V. Nadenau, and H.W. Schock, Journal of Applied Physics, Vol. 87, No. 1, pp. 594-602, 2000.

[22] A. Bauknecht, U. Blieske, T. Kampschulte, J. Albert, H. Sehnert, M.Ch. Lux-Steiner, A. Klein, and W. Jaegermann, Applied Physics Letters, Vol. 74, No. 8, pp. 1099-1101, 1999.

[23] S. Siebentritt, A. Bauknecht, A. Gerhard, U. Fiedeler, T. Kampschulte, S. Schuler, W. Harneit, S. Brehme, J. Albert, and M.Ch. Lux-Steiner, Solar Energy Materials & Solar Cells, Vol. 67, pp. 129-136, 2001.

[24] M. Rusu, S. Sadewasser, Th. Glazel, P. Gashin, A. Simashkevich, and A. Jäger-Waldau, Thin Solid Films, Vol. 403-404, pp. 344-348, 2002.

[25] A. Bauknecht, U. Blieske, T. Kampschulte, A. Enaoui, V. Nadenau, H.W. Schock, A.N. Tiwari, M. Krejci, S. Duchemin, M.C. Artaud, L.M. Smith, S. Rushworth, J. Söllner, and M.C. Lux-Steiner, Proceedings of the 2nd World Conference and Exhibition on Photovoltaic Solar Energy Conversion, Vienna, Austria, pp. 2436-2439, 1998.

[26] J. Klaer, J. Bruns, R. Henninger, K. Siemer, R. Klenk, K. Ellmer, and D. Bräunig, Semiconductor Science and Technology, Vol. 13, No. 12, pp. 1456-1458, 1998.

[27] B. Tell, J.L. Shay, and H.M. Kasper, Physical Review B (Solid State), Vol. 4, No. 8, pp. 2463-2471, 1971.

[28] R. Scheer, K. Diesner, and H.-J. Lewerenz, Thin Solid Films, Vol. 168, pp. 130-136, 1995.

[29] D. Braunger, T. Hariskos, C. Köble, T. Walter, N. Wieser, and H.W. Schock, Conference Record of the 25th IEEE Photovoltaic Specialists Conference, Washington, DC, pp. 1001-1004, 1996.

[30] K. Siemer, J. Klaer, I. Luck, J. Bruns, R. Klenk, and D. Bräunig, Solar Energy Materials & Solar Cells, Vol. 67, pp. 159-166, 2001.

[31] I. Hengel, A. Neisser, R. Klenk, and M.Ch. Lux-Steiner, Thin Solid Films, Vol. 361-362, pp. 458-462, 2000.

[32] A.M. Chaparro, C. Maffiotte, M.T. Gutiérrez, J. Herrero, J. Klaer, K. Siemer, and D. Bräunig, Thin Solid Films, Vol. 387, pp. 104-107, 2001.

[33] A.M. Chaparro, M.T. gutiérrez, J. Herrero, J. Klaer, M.J. Romero, and M.M. Al-Jassim, Progress in Photovoltaics: Research and Applications, Vol. 10, pp. 465-480, 2002.

[34] M.Ch. Lux-Steiner, A. Ennaoui, Ch.-H. Fischer, A. Jäger-Waldau, J. Klaer, R. Klenk, R. Könenkamp, Th. Matthes, R. Scheer, S. Siebentritt, and A. Weidinger, Thin Solid Films, Vol. 361-362, pp. 533-539, 2000.

[35] L.K. Samanta, D.K. Ghosh, and G.C. Bhar, Physical Review B, Vol. 35, No. 9, pp. 4519-4521, 1987.

[36] S.H. Wei and A. Zunger, Journal of Applied Physics, Vol. 78, No. 6, pp. 3846-3856, 1995.

[37] H.S. Soliman, Journal of Physics D (Applied Physics), Vol. 31, No. 13, pp. 1516-1521, 1998.

[38] J. González, E. Calderón, T. Tinoco, J.P. Itié, A. Polian, and E. Moya, Journal of the Physics and Chemistry of Solids, Vol. 56, No.3/4, pp. 507-516, 1995.

[39] J. González, E. Calderón, F. Capet, and F. Baert, Physical Review B (Condensed Matter), Vol. 58, No. 20, pp. 13654-13659, 1998.

[40] K. Hara, T. Shinozawa, J. Yoshino, and H. Kukimoto, Journal of Crystal Growth, Vol, 93, pp. 771-775, 1988.

[41] D. Schmid, M. Ruckh, F. Grunwald, and H.W. Schock, Journal of Applied Physics, Vol. 73, No. 6, pp. 2902-2909, 1993.

[42] R. Herberholz, V. Nadenau, U. Rühle, C. Köble, H.W. Schock, and B. Dimmler, Solar Energy Materials and Solar Cells, Vol. 49, pp. 227-237, 1997.

[43] K.T. Ramakrishna Reddy and P. Jayarama Reddy, Journal of Physics D (Applied Physics), Vol. 25, No. 9, pp. 1345-1348, 1992.

[44] A. Ennaoui, S. Siebentritt, M.Ch. Lux-Steiner, W. Riedl, and F. Karg, Solar Energy Materials & Solar Cells, Vol. 67, pp. 31-40, 2001.

[45] A. Ennaoui, M. Weber, M. Saad, W. Harneit, M.Ch. Lux-Steiner, and F. Karg, Thin Solid Films, Vol. 361-362, pp. 450-453, 2000.

[46] C.D. Lokhande, P.S. Patil, H. Tributsch, and A. Ennaoui, Solar Energy Materials and Solar Cells, Vol. 55, pp. 379-393, 1998.

[47] Martha Symko-Davies, 19th European Photovoltaic Solar Energy Conference and Exhibition, Paris, France, 2004.

[48] R. Herberholz, M. Igalson, and H.W. Schock, Journal of Applied Physics, Vol. 83, No. 1, pp. 318-325, 1998.

[49] U. Rau, D. Braunger, R. Herberholz, H.W. Schock, J.-F. Guillemoles, L. Kronik, and D. Cahen, Journal of Applied Physics, Vol. 86, No. 1, pp. 497-505, 1999.

[50] T. Walter, R. Herberholz, and H.W. Schock, Diffusion and Defect Data Part B (Solid State Phenomena), Vol. 51-52, pp. 309-315, 1996.

[51] F. Engelhardt, M. Schmidt, Th. Meyer, O. Seifert, J. Parisi, and U. Rau, Physics Letters A, Vol. 245, No. 5, pp. 489-493, 1998.

[52] R. Herberholz, V. Nadenau, U. Rühle, C. Köble, H.W. Schock, and B. Dimmler, Solar Energy Materials and Solar Cells, Vol. 49, No. 1-4, pp. 227-237, 1997.

[53] H. Zhu, A.K. Kalkan, J. Hou, and S.J. Fonash, AIP Conference Proceedings, Denver, CO, Vol. 462, pp. 309-314, 1999.

[54] H. Zhu and S.J. Fonash, Proceedings of the Materials Research Society Symposium, San Francisco, CA, Vol. 507, pp. 395-402, 1998.

[55] T. Walter, R. Menner, M. Ruckh, L. Kaser, and H.W. Schock, Conference Record of the 22nd IEEE Photovoltaic Specialist Conference, Las Vegas, NV, pp. 924-929, 1991.

[56] T. Dullweber, G. Hanna, U. Rau, and H.W. Schock, Solar Energy Materials & Solar Cells, Vol. 67, pp.145-150, 2001.

[57] H. Koremer, RCA Review, Vol. 18, p. 332, 1957.

[58] C.H. Huang, S.S. Li, and T.J. Anderson, Conference Record of the 29th IEEE Photovoltaic Specialists Conference, New Orleans, LA, pp. 748-751, 2002.

[59] M.A. Contreras, B. Egaas, K. Ramanathan, J. Hiltner, A. Swartzlander, F. Hasoon, and R. Noufi, Progress in Photovoltaics: Research & Application, Vol. 7, pp. 311-316, 1999.

[60] A division of the national center for photovoltaics at the national renewable energy laboratory, measurements & characterization, http://www.nrel/measurements/voltage.html, 2003.

[61] T. Dullweber, G. Hanna, W. Shams-Kolahi, A. Schwartzlander, M.A. Contreras, R. Noufi, and H.W. Schock, Thin Solid Films, Vol. 361-362, pp. 478-481, 2000.

[62] T. Dullweber, U. Rau, M.A. Contreras, R. Noufi, and H.W. Schock, IEEE Transactions on Electron Devices, Vol. 47, No. 12, pp. 2249-2254, 2000.

[63] A. Dhingra and A. Rothwarf, Conference Record of the 23rd IEEE Photovoltaic Specialist Conference, Louisville, KY, pp. 475-480, 1993.

[64] D. Albin, J. Tuttle, J. Goral, A. Mason, R. Noufi, and S.H. Risbud, Conference Record of the 20th IEEE Photovoltaic Specialists Conference, Las Vegas, NV, pp. 1495-1499, 1988.

[65] J.H. Schön and E. Bucher, Solar Energy Materials & Solar Cells, Vol. 57, pp. 229-237, 1999.

[66] M. Saad, H. Riazi, E. Bucher, and M.Ch. Lux-Steiner, Applied Physics A, Vol. 62, pp. 181-185, 1996.

[67] J.A. Hutchby, R.J. Markunas, and S.M. Bedair, SPIE, Photovoltaics, Vol. 543, pp. 40-61, 1985.

[68] E.D. Jackson, Proceedings for the Conference on the Use of Solar Energy, Tuscon, pp. 122-126, 1955.

[69] J.M. Doña and J. Herrero, 12th European Photovoltaic Solar Energy Conference, Amsterdam, Netherlands, p. 597, 1994.

[70] D. Lincot, R. Ortega-Borges, and M. Froment, Applied Physics Letters, Vol. 64, No. 5, pp. 569-571, 1994.

[71] J.M. Doña and J. Herrero, Thin Solid Films, Vol. 268, pp. 5-12, 1995.

[72] B. Mokili, Y. Charreire, R. Cortes, and D. Lincot, Thin Solid Films, Vol. 288, No. 1-2, pp. 21-28, 1996.

[73] P.K. Nair and M.T.S. Nair, Semiconductor Science and Technology, Vol. 7, No. 2, pp. 239-244, 1992.

[74] J.M. Doña and J. Herrero, Journal of the Electrochemical Society, Vol. 141, No. 1, pp. 205-210, 1994.

[75] C. Platzer-Bjorkman, L. Stolt, and J. Kessler, Proceedings of the Estonian Academy of Sciences. Physics, Mathematics Vol. 52, No. 3, pp. 299-307, 2003.

[76] E.Y.M. Lee, N.H. Tran, R.N. Lamb, and J.J. Russell, Journal of Physical Chemistry B, Vol. 107, No. 22, pp. 5208-5211, 2003.

[77] K.A. Dhese, J.E. Nicholls, W.E. Hagston, P.J. Wright, B. Cockayne, and J.J. Davies, Journal of Crystal Growth, Vol. 138, No. 1-4, pp. 140-144, 1994.

[78] K.P. O`Donnel, P.J. Parbrook, B. Henderson, C. Trager-Cowan, X. Chen, F. Yang, M.P. Halsall, P.J. Wright, B. Cockayne, Journal of Crystal Growth, Vol. 101, No. 1-4, pp. 554-558, 1990.

[79] Y.F. Nicolau and J.C. Menard, Journal of Crystal Growth, Vol. 92, No. 1-2, pp. 128-142, 1988.

[80] Y.F. Nicolau, M. Dupuy, and M. Brunel, Journal of the Electrochemical Society, Vol. 137, No. 9, pp. 2915-2924, 1990.

[81] R. Mikami, H. Miyazaki, T. Abe, A. Yamada, and M. Konagai, 3rd World Conference on Photovoltaic Energy Conversion, Osaka, Japan, pp. 519-522, 2003.

[82] C. Platzer-Bjőrkman, J. Kessler, and L. Stolt, 3rd World Conference on Photovoltaic Energy Conversion, Osaka, Japan, pp. 461-464, 2003.

[83] S. Damaskinos, J. E. Phillips, M. Roy, and R. W. Birkmire, Canadian Journal of Physics, Vol. 67, pp. 420-424, 1989.

[84] M. A. Contreras, T. Nakada, M. Hongo, A. O. Pudov, and J. R. Sites, 3rd World Conference on Photovoltaic Energy Conversion, Osaka, Japan, pp. 570-573, 2003.

[85] K. Kushiya, M. Tachiyuki, T. Kase, I. Sugiyama, Y. Nagoya, D. Okumura, M. Sato, O. Yamase, and H. Takeshita, Solar Energy Materials and Solar Cells, Vol. 49, pp. 277-283, 1997.

[86] K.T. Ramakrishna Reddy, H. Gopalaswamy, and P. Jayarama Reddy, Vacuum, Vol. 43, No. 8, pp. 811-815, 1992.

[87] T. Yamaguchi, Y. Yamamoto, T. Tanaka, Y. Demizu, and A. Yoshida, Thin Solid Films, Vol. 281-282, pp. 375–378, 1996.

[88] A.M. Salem, Applied Physics A, Vol. A74, No. 2, pp. 205-211, 2002.

[89] N. Romeo, G. Sberveglieri, and L. Tarricone, Applied Physics Letters, Vol. 32, No. 12, pp. 807-809, 1978.

[90] Y. Hashimoto, N. Kohara, T. Negami, M. Nishitani, and T. Wada, Japanese Journal of Applied Physics, Part 1, Vol. 35, No. 9A, pp. 4760-4764, 1996.

[91] K. Ramanathan, M.A. Contreras, C.L. Perkins, S. Asher, F.S. Hasoon, J. Keane, D. Young, M. Romero, W. Metzger, R. Noufi, J. Ward, and A. Duda, Progress in Photovoltaics: Research and Applications, Vol. 11, pp. 225-230, 2003.

[92] J. Stankiewicz and W. Giriat, Applied Physics Letters, Vol. 35, No. 1, pp. 70-71, 1979.

[93] N. Romeo, G. Sberveglieri, L. Tarricone, and C. Paorici, Applied Physics Letters, Vol. 30, No. 2, pp. 108-110, 1977.

[94] M. Saad, H. Riazi-Nejad, E. Bucher, and M.Ch. Lux-Steiner, Conference Record of the First World Conference on Photovoltaic Energy Conversion, Waikoloa, HI, pp. 214-217, 1994.

[95] K.T.R. Reddy and P.J. Reddy, Materials Letters, Vol. 10, No, 6, pp. 275-279, 1990.

[96] R. Klenk, R. Mauch, R. Schäffler, D. Schmid, and H.W. Schock, Conference Record of the 22nd IEEE Photovoltaic Specialists Conference, Las Vegas, NV, pp. 1071-1076, 1991.

[97] V. Nadenau, D. Hariskos, and H.W. Schock, Proceedings of the 14th European Photovoltaic Solar Energy Conference, Bedford, U.K., p. 1250, 1997.

[98] W.N. Shafarman, R. Klenk, and B.E. McCandless, Conference Record of the 25th IEEE Photovoltaic Specialist Conference, Washington, DC, pp. 763-768, 1996.

[99] G. Sasikala, P. Thilakan, and C. Subramanian, Solar Energy Materials & Solar Cells, Vol. 62, pp. 275-293, 2000.

[100] S. Yamaga, A. Yoshikawa, and H. Kasai, Journal of Crystal Growth, Vol. 99, pp. 432-436, 1990.

[101] K. Nishimura, K. Sakai, Y. Nagao, and T. Ezaki, Journal of Crystal Growth, Vol. 117, pp. 119-124, 1992.

BIOGRAPHICAL SKETCH

The author, Jiyon Song, was born in Chongju, Korea. She received a Bachelor of Science degree and a Master of Science degree from the Department of Physics at the Chungbuk National University, Korea, in 1992 and 1994. Since 2002, she has been a research assistant in the Optoelectronics Laboratory at the University of Florida, under Dr. Sheng S. Li's guidance. In December 2002, she was awarded a Master of Science degree in electrical and computer engineering from the University of Florida. After her graduation, she continued to work toward her Ph.D. degree. Her research interests include modeling and simulation of CIGS-based tandem solar cells, fabrication and electrical characterization of CIGS-based thin-film solar cells, and thin-film characterizations.

I certify that I have read this study and that in my opinion it conforms to acceptable standards of scholarly presentation and is fully adequate, in scope and quality, as a dissertation for the degree of Doctor of Philosophy.

Sheng S. Li, Chairman
Professor of Electrical and Computer
Engineering

I certify that I have read this study and that in my opinion it conforms to acceptable standards of scholarly presentation and is fully adequate, in scope and quality, as a dissertation for the degree of Doctor of Philosophy.

Gijs Bosman
Professor of Electrical and Computer
Engineering

I certify that I have read this study and that in my opinion it conforms to acceptable standards of scholarly presentation and is fully adequate, in scope and quality, as a dissertation for the degree of Doctor of Philosophy.

Timothy J. Anderson
Professor of Chemical Engineering

I certify that I have read this study and that in my opinion it conforms to acceptable standards of scholarly presentation and is fully adequate, in scope and quality, as a dissertation for the degree of Doctor of Philosophy.

Paul Holloway
Distinguished Professor of Materials
Science and Engineering

This dissertation was submitted to the Graduate Faculty of the College of Engineering and to the Graduate School and was accepted as partial fulfillment of the requirements for the degree of Doctor of Philosophy.

August 2006

Pramod Khargonekar

Pramod P. Khargonekar
Dean, College of Engineering

Kenneth J. Gerhardt
Interim Dean, Graduate School